Applied Catalysis B: Environmental 300 (2022) 120720

Contents lists available at ScienceDirect

Applied Catalysis B: Environmental

journal homepage: www.elsevier.com/locate/apcatb

Looking inside a Ni-Fe/$MgAl_2O_4$ catalyst for methane dry reforming via Mössbauer spectroscopy and in situ QXAS

Valentijn De Coster [a], Nadadur Veeraraghavan Srinath [a], Stavros Alexandros Theofanidis [b,1], Laura Pirro [a], Antoine Van Alboom [c], Hilde Poelman [a,*], Maarten K. Sabbe [a], Guy B. Marin [a], Vladimir V. Galvita [a]

[a] Laboratory for Chemical Technology, Ghent University, Technologiepark 125, B-9052 Ghent, Belgium
[b] Laboratory of Petrochemical Technology, Chemical Engineering Department, Aristotle University of Thessaloniki, 54124 Thessaloniki, Greece
[c] Department of Applied Physics, Ghent University, Valentin Vaerwyckweg 1, B-9000 Ghent, Belgium

ARTICLE INFO

Keywords:
Ni-Fe alloy
X-ray absorption spectroscopy
MCR-ALS
CO_2 re-oxidation

ABSTRACT

The evolution of the constituents of an 8 wt%Ni-5 wt%Fe/$MgAl_2O_4$ catalyst for dry reforming of methane (DRM) is monitored by in situ quick X-ray absorption spectroscopy (QXAS) and ^{57}Fe Mössbauer spectroscopy. In as prepared state, Fe is present as $NiFe_2O_4$ at the surface and as $MgFe^{3+}{}_xAl_{2-x}O_4$ within the support, whereas Ni is mainly present as NiO. During H_2-TPR, $NiFe_2O_4$ and NiO form an alloy from 500 °C on and $MgFe^{3+}{}_xAl_{2-x}O_4$ is partially reduced to $MgFe^{2+}{}_xAl_{2-x}O_4$, such that Ni-Fe alloy, $MgFe^{2+}{}_xAl_{2-x}O_4$ and $MgFe^{3+}{}_xAl_{2-x}O_4$ are the prevalent phases in the reduced catalyst. During DRM, dominantly oxidizing environments ($CH_4/CO_2 = 1/2$, 1/1.5) lead to formation of FeO_x nanoparticles at the surface of the Ni-Fe alloy, thereby affecting the DRM activity, and possibly to some reincorporation of Fe into the support. For $CH_4/CO_2 = 1/1$, no significant changes occur in the catalyst's activated state, as a consequence of reduction by CH_4 dissociation species counteracting oxidation by CO_2. However, Mössbauer analysis detects continued extraction of Fe from the support, sustaining ongoing Ni-Fe alloying.

1. Introduction

DRM, represented in Eq. (1), is of major interest for sustainable development as it entails the catalytic conversion of the greenhouse gases CO_2 and CH_4 to CO and H_2, i.e. syngas, which can serve as building blocks in the creation of high-value end products, e.g. via Fischer Tropsch [1,2] or methanol synthesis processes [3,4].

$$CO_2 + CH_4 \rightarrow 2H_2 + 2CO \quad \Delta H^\circ = 261 \quad \text{kJ} \quad \text{mol}^{-1} \tag{1}$$

As global supply of natural gas has increased tremendously [5], methane has become an economically interesting co-reactant for CO_2 conversion, making DRM an even more attractive pathway for CO_2 utilization. DRM has a low operating cost compared to other methane reforming processes such as steam reforming [6,7], autothermal reforming [8,9] and partial oxidation of methane [10,11].

Despite its advantages, different obstacles impede the industrial exploitation of DRM. The high endothermicity of Eq. (1) requires the use of high temperatures (650–850 °C). With equimolar CH_4 and CO_2 concentrations, i.e. industrially relevant feed composition, this promotes catalyst deactivation due to coke formation and sintering of the support and metal particles [12–14]. It is therefore mandatory that an efficient DRM catalyst is thermally stable and resistant to coke formation and sintering, whilst also being highly active and cost-effective.

Ni-Fe catalysts have proved successful in meeting the above criteria, leading to a rise in the application of these materials in reforming reactions. Wang et al. [15] studied Ni-Fe/Al_2O_3 for steam reforming of biomass-derived tar, and concluded that the catalyst displayed an enhanced performance over monometallic Ni and Fe counterparts. This was attributed to the formation of a Ni-Fe alloy, wherein synergy between Ni as tar activation site and Fe as oxygen carrier that oxidizes the carbon species formed on neighboring Ni sites decreases coke accumulation. Analogous Ni-Fe synergistic effects have been reported in methanation [16], chemical looping [17] and furfural conversion [18] catalysts. Kim and co-workers [19] compared monometallic Ni, Fe and

* Correspondence to: Laboratory for Chemical Technology, Ghent University, Technologiepark 125, 9052 Ghent, Belgium.
E-mail address: Hilde.Poelman@UGent.be (H. Poelman).
[1] Present address: Department of Chemical Engineering, Aristotle University of Thessaloniki, University Campus, 54124 Thessaloniki, Greece

https://doi.org/10.1016/j.apcatb.2021.120720
Received 8 July 2021; Received in revised form 8 September 2021; Accepted 10 September 2021
Available online 14 September 2021
0926-3373/© 2021 Elsevier B.V. All rights reserved.

bimetallic Ni-Fe catalysts on a hydrotalcite-derived $Mg_xAl_yO_z$ support for DRM at 650 °C, and found that catalysts with Ni/(Fe+Ni) = 0.8 displayed the highest activity and stability. Ex situ and in situ characterization showed the redox functionality of the Fe species suppressed carbon formation in DRM. These results are in accordance with the work of Theofanidis et al. [20], who attributed the coke resistance in Ni-Fe/$MgAl_2O_4$ DRM catalysts to the formation of FeO_x at the alloy surface, which react via a redox mechanism with the deposited carbon.

In spite of these studies, questions remain as to the nature of the phases present in these Ni-Fe reforming catalysts after reduction/activation and during reaction. Using operando XAS, Kim and co-workers [19] observed the formation of FeO in hydrotalcite-derived Ni-Fe/$Mg_xAl_yO_z$ during DRM at 650 °C and 1 atm and equimolar CH_4 and CO_2 concentrations. For spinel-supported Ni-Fe/$MgAl_2O_4$, the formation of FeO_x has only been confirmed via in situ X-ray diffraction (XRD) during DRM (at 750 °C and 1 atm) at conditions with relatively high CO_2 partial pressures, i.e. $CH_4/CO_2 \leq 1/6$ [20]. At feed compositions closer to equimolar CH_4 and CO_2 concentrations, which are of high industrial importance, these oxides cannot be detected by diffraction. Hence, it is unclear whether this is because (i) such oxide phase indeed does not form in Ni-Fe/$MgAl_2O_4$ under such conditions, (ii) the corresponding crystallites are too small for detection via XRD, or (iii) their concentrations are too low for detection via this technique. The presence of FeO is of particular importance as the latter was found to be at the origin of enhanced sintering given its low Tamman temperature [21].

Another matter worthy of investigation is the Ni-Fe alloy formation process during catalyst activation. Due to the overlapping nature of characteristic diffraction peaks, the presence of NiO, γ-Fe_2O_3, or $NiFe_2O_4$ cannot be confirmed beyond doubt by XRD studies [20]. In addition, dominant contributions of $MgAl_2O_4$ prevent detection of a possible $NiAl_2O_4$ phase. Moreover, spinel supports like $MgAl_2O_4$ can incorporate Fe, typically following one pot co-precipitation synthesis [22–24], yielding contributions related to Fe-substituted $MgAl_2O_4$ phases. For the present Ni-Fe/$MgAl_2O_4$ impregnated catalysts however, such Fe-incorporated support phase lacks confirmation. Resolving these uncertainties will allow a better understanding of the behavior of these catalysts under DRM reaction conditions and lay the path towards improved catalyst synthesis.

In the present work, the above structural questions are addressed by means of a QXAS study of a $MgAl_2O_4$-supported DRM catalyst with 8 wt % Ni and 5 wt% Fe, hereafter called 8Ni5Fe/$MgAl_2O_4$. This Ni/Fe ratio was chosen as it shows optimal activity and stability, with limited sintering and low carbon formation [20]. To characterize the sample during reaction, in situ QXAS [25] is employed at the Ni K and Fe K edge, both for H_2-TPR and DRM under industrially relevant conditions, i.e. CH_4/CO_2 = 1/1, 750 °C and GHSV = 4580 h^{-1}. Speciation of time-resolved XAS data is performed by means of statistical analysis via principal component analysis (PCA) and multivariate curve resolution coupled with alternating least squares (MCR-ALS). The analysis of the QXAS data is complemented with both transmission and surface-sensitive ^{57}Fe Mössbauer spectroscopy in as prepared state, i.e. after calcination, as well as after H_2-TPR and after DRM.

2. Materials and methods

2.1. Catalyst preparation

$MgAl_2O_4$ support was produced via coprecipitation of Al$(NO_3)_3$.9 H_2O (ACS reagent, ≥98%, Sigma-Aldrich) and Mg$(NO_3)_2$.6 H_2O (≥99%, Sigma-Aldrich) as described in the work of Theofanidis et al. [20]. To acquire metal loadings of 8 wt% Ni and 5 wt% Fe, appropriate amounts of the corresponding nitrates were used in an incipient wetness impregnation method. Details on the catalyst preparation and preliminary characterization of composition have been reported previously [20].

2.2. XAS references preparation

Fe^{3+}-substituted $MgAl_2O_4$ ($MgFe^{3+}AlO_4$) with 10 wt% Fe content was prepared via coprecipitation of Al$(NO_3)_3$.9 H_2O (ACS reagent, ≥98%, Sigma-Aldrich), Mg$(NO_3)_2$.6 H_2O (≥99%, Sigma-Aldrich) and Fe$(NO_3)_3$.9 H_2O (≥99.95%, Sigma-Aldrich) as reported by Dharanipragada et al. [23]. $NiFe_2O_4$ and $NiAl_2O_4$ references were synthesized through a sol-gel autocombustion method. In a typical synthesis, 0.551 g Ni$(NO_3)_2$.6 H_2O (99.999%, Sigma-Aldrich) (1.90 mmol) was put to a 100 mL glass beaker containing 7 mL deionized water. Then, the appropriate quantity of Al$(NO_3)_3$.9 H_2O (ACS reagent, ≥98%, Sigma-Aldrich) or Fe$(NO_3)_3$.9 H_2O (≥99.95%, Sigma-Aldrich) was added to obtain a molar ratio of Ni/Al (or Ni/Fe) of 1/2, as well as citric acid (ACS reagent, ≥99.5%, Sigma-Aldrich), such that $n_{citric\ acid}/n_{nitrates}$ = 1/1. The aqueous solution was magnetically stirred at 50 °C at 350 rpm, and 50 mg of polyvinylpyrrolidone (PVP; average mol weight 40,000, Sigma-Aldrich) was added. The mixture was left to stir at constant temperature until all PVP was dissolved, after which the temperature was increased to 100 °C and maintained until a transparent gel was formed. This gel was dried overnight at 120 °C, yielding a powder that was first calcined under air flow at 400 °C (3 °C/min) for 1 h, and further up to 1000 °C (3 °C/min) with a 1 h dwell time.

2.3. Characterization techniques

2.3.1. QXAS measurements

In situ transmission QXAS measurements were performed at the ROCK beamline of the French synchrotron SOLEIL [26]. The storage ring was operated at 2.75 GeV with a ring current of 500 mA in top-up mode. A Frahm monochromator [25] equipped with a Si(111) channel-cut crystal oscillated at 2 Hz and scanned both the Fe K (7112 eV) and Ni K (8333 eV) edges, using a macro for fast edge switching. This resulted in quasi-simultaneous acquisition of both edges, with a delay of ~60 s. Catalytic samples of approximately 5 mg, ground to powders and 50% diluted with boron nitride, were inserted into a 2 mm quartz capillary reactor in between two quartz wool plugs. The capillary reactor was implemented in a frame which was connected to gas feed lines through Swagelok fittings. The inlet gas flow rates were maintained by means of calibrated Brooks mass flow controllers and a total flow between 10 and 60 NmL/min was employed. An external, calibrated heat gun was used to reach reaction temperatures up to 800 °C. XAS spectra energy calibration was assured by the measurement of Ni and Fe foils.

H_2-TPR experiments were performed by subjecting the sample to a heating rate of 10 °C/min from 20 °C to a maximum of 800 °C, with a holding time of 30 min, under a flow of 10 NmL/min of 5 V% H_2 in He. After this reduction program, an in situ DRM measurement was performed with a molar CH_4/CO_2 ratio of 1/2 (2.6 NmL He/min, 4.2 NmL CH_4/min and 8.4 NmL CO_2/min) at 750 °C and 1 atm for 30 min. Following this DRM measurement, the catalyst was regenerated, i.e. brought back into its metallic state, by an isothermal H_2 reduction (5 V% H_2 in He, 15 NmL/min) at 750 °C for 30 min, after which it was subjected to a second DRM measurement with a molar CH_4/CO_2 ratio of 1/1.5 (3.0 NmL He/min, 4.6 NmL CH_4/min and 6.8 NmL CO_2/min) at 750 °C and 1 atm for 30 min. Following regeneration by an isothermal H_2 treatment, a final in situ DRM measurement was carried out for a molar CH_4/CO_2 ratio of 1/1 (3.0 NmL He/min, 5.0 NmL CH_4/min and 5.0 NmL CO_2/min), also at 750 °C and 1 atm for 30 min. For ease of expression, the identity $R_c = CH_4/CO_2$ will be used hereafter.

The same setup was used for ex situ measurements of reference samples. Oxidized state references for Fe and Ni were obtained via measurements of pelletized α-Fe_2O_3, γ-Fe_2O_3, $NiFe_2O_4$, $MgFe^{3+}AlO_4$, Fe_3O_4, FeO, $NiAl_2O_4$ and NiO.

20 consecutive scans of the in situ QXAS data were averaged to increase the signal to noise ratio. All recorded data were normalized via the Python normalization GUI created by O. Roudenko [27]. Linear combination fitting (LCF) of the normalized XANES spectra of the as

prepared catalyst was performed using the associated module in the Athena software [28]. Analysis was restricted to the energy regions [7111 – 7161] eV and [8327 – 8377] eV for Fe K and Ni K edge data, respectively.

For the purpose of speciating the different Ni and Fe species through MCR-ALS analysis of the QXAS datasets, the number of principal components in each QXAS dataset was assessed through PCA [29,30]. With this number of components, the MCR-ALS analysis was performed through the MATLAB® toolbox developed by Jaumot et al. [31]. Initial guesses for MCR-ALS were spectral type, obtained via the toolbox's built-in PURE initial estimation method [31]. MCR-ALS analyses encompassed the full recorded energy range of the XAS spectra. The principle of the MCR-ALS methodology, as well as more detailed information on the MCR-ALS analyses are provided in the Supporting Information section (Figs. S1 and S2, and related text).

2.3.2. ^{57}Fe Mössbauer spectroscopy

Transmission ^{57}Fe Mössbauer spectra (TMS) of 8Ni5Fe/$MgAl_2O_4$ were collected for the as prepared state, after H_2-TPR (10 °C/min, up to 800 °C, 30 min) and after DRM (750 °C, 1 atm, 30 min) for $R_c = 1/2$ and 1/1 at room temperature (RT; 20 °C). For the as prepared state, additional TMS were recorded at −193 °C to obtain better data quality. For surface-sensitive measurements, integrated low-energy electron Mössbauer spectra [32] (ILEEMS) were collected at RT for the as prepared, reduced and spent samples. These ILEEMS were recorded with sample and electron detector (channeltron) contained in a high-vacuum chamber. A bias voltage of + 146 V was applied to the channeltron with respect to the sample holder.

All spectra were recorded in 1024 channels with a velocity scale of approximately ± 10 mm/s. The spectrometer operated in constant acceleration mode with a triangular reference signal and had excellent linearity. A ^{57}Co(Rh) source was used, but, center shift values δ reported hereafter are referenced with respect to α-Fe at RT. The TMS velocity calibration was based on a RT spectrum of standard hematite (α-Fe_2O_3), while for ILEEMS it was based on the RT spectrum of an enriched ^{57}Fe foil. For both types of Mössbauer spectroscopy, the velocity (v) increment per channel was 0.0456 ± 0.0001 mm/s. The full line width at half maximum of the inner lines of the calibration spectrum was 0.254 ± 0.002 mm/s. Accumulation of TMS and ILEEMS data took several days until a background of at least 10^6 and 10^5 counts per channel was reached, respectively.

The Mössbauer spectra were fitted with appropriate combinations of Lorentzian profiles representing quadrupole and sextet components, and spectral parameters of these components (center shift (δ), quadrupole splitting (ΔE_Q), full line width at half maximum (Γ), quadrupole shift ($2\varepsilon_Q$) and magnetic hyperfine field (H_{hf})) were determined. These yield information regarding the interactions between the ^{57}Fe nuclei and their electronic and magnetic environment. In turn, this was used to identify the related Fe phases.

3. Results and discussion

3.1. Speciation of the as prepared state

3.1.1. XAS spectra – as prepared

The XANES spectra at the Fe K and Ni K edge of the as prepared catalyst are presented in Fig. 1. Comparison of the XANES features of the catalyst's initial Fe species with those of reference spectra of γ-Fe_2O_3, $MgFe^{3+}AlO_4$ and $NiFe_2O_4$ (Fig. 1A) reveals an overall Fe^{3+} oxidation state in the sample, as indicated by the similar edge and white line (WL) position. In addition, all Fe K spectra display a pre-edge peak, which is indicative of forbidden quadrupolar 1 s → 3d transitions and d-p orbital mixing associated with dipolar transitions [33]. While all Fe^{3+} reference spectra bear resemblance with the catalyst's as prepared state regarding the shape of the pre-edge and WL features, differences are observed in their intensity. An LCF analysis (Fig. S3) estimates contributions of ~48% $NiFe_2O_4$ and ~52% $MgFe^{3+}AlO_4$, while γ-Fe_2O_3 is not resolved.

The as prepared state's Ni K edge position indicates an overall Ni^{2+} oxidation state (Fig. 1B). The pre-edge features for the Ni species largely overlap with those of NiO in terms of shape, position and intensity. However, the catalyst's WL position is found ~0.7 eV higher than that of said NiO reference. While the WL position is closer to that of $NiFe_2O_4$ (~0.3 eV lower) than that of $NiAl_2O_4$ (~0.9 eV lower), the catalyst's pre-edge feature has little resemblance with the former.

Though it is known that discrepancies between reference and catalytic samples can arise from inherent differences in electronic and structural properties between the 'bulk' powder references and the actual catalyst, this mostly has limited effect on the XANES features. It is thus more likely that the observations in Fe K spectra are the result of a combination of spectral contributions of Fe phases. As such, discrepancies observed in the Ni K spectra could be ascribed to the presence of Ni species in NiO, apart from contributions of $NiFe_2O_4$ [34] and/or $NiAl_2O_4$ [35]. In accordance, LCF of the as prepared state (Fig. S4) indicates contributions of ~78% NiO, with the remaining ~22% belonging to $NiFe_2O_4$.

3.1.2. Mössbauer spectroscopy – as prepared

To further specify the nature of Fe in the as prepared catalyst, TMS and ILEEMS were performed. At RT (Fig. S5), a poorly developed magnetic six-line component superimposed on a doublet is noticed. Fitting with a combination of a model-independent quadrupole-splitting distribution (QSD) and a magnetic hyperfine-field distribution (HFD) yields a relative area (RA) ~0.33 for the contribution of the magnetic component to the total spectrum. The hyperfine parameters of both the sextet and doublet component are ill-defined and not conclusive as to the nature of the material.

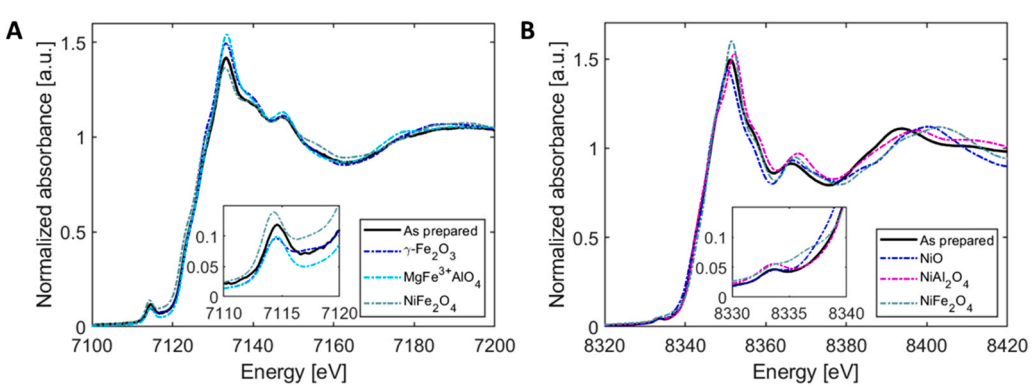

Fig. 1. XANES spectra of as prepared 8Ni5Fe/$MgAl_2O_4$ and selected oxide references at (A) the Fe K edge and (B) the Ni K edge. Reference spectra are shown for comparative purposes. The insets show zooms of the pre-edge features.

At −193 °C (Fig. 2A), the sextet component is more pronounced and a similar fit using a QSD and a HFD yields an RA value of ~0.41 for the magnetic contribution, which is not drastically higher than the RA value at RT. The involved magnetic phase likely possesses a broad transition-temperature range close to RT, implying that at RT the magnetic hyperfine field exhibits a wide distribution and that a fraction of that phase may even be (super)paramagnetic and contribute to the doublet component [36].

At cryogenic temperature, the average hyperfine field ($H_{hf,av}$) of the magnetic phase is 473 kOe and the maximum-probability field ($H_{hf,m}$) 486 kOe. There is no obvious fine structure in the calculated distribution profile for the hyperfine field ($p(H_{hf})$). The average isomer shift is found to be 0.38 mm/s and the quadrupole shift is zero within experimental error limits. These data are consistent with a magnetic phase due to an (Fe,Ni)-rich spinel phase [37], presumably $NiFe_2O_4$.

The doublet component in the low-temperature spectrum is adequately described by a QSD with lower and upper limit for ΔE_Q of 0.20 and 1.60 mm/s, respectively. The average isomer shift amounts to $\delta = 0.39$ mm/s, suggesting trivalent Fe in mixed octahedral O_6 and tetrahedral O_4 coordination. From the calculated probability distribution profile, $p(\Delta E_Q)$ (Fig. S6), an average value for ΔE_Q of ~0.90 mm/s is found. However, the distribution is clearly bimodal, confirming the presence of Fe^{3+} at two different crystallographic sites of the involved Fe-containing phase. This non-magnetic phase can be ascribed to an Fe^{3+}-substituted $MgAl_2O_4$ spinel [38], proving that impregnation of Fe onto $MgAl_2O_4$ can lead to its partial incorporation upon calcination. Fe then undergoes interaction with the support, creating spinels of the type $MgFe^{3+}{}_xAl_{2-x}O_4$, where x varies between 0 and 1. Prior studies [23] have only reported Fe^{3+} in octahedral positions, whereas the current sample has mixed octahedral and tetrahedral coordination. This can relate to the incipient wetness impregnation of Fe and Ni on the $MgAl_2O_4$ support used in the preparation of this sample, which is in contrast to other works, wherein the Fe, Mg and Al precursors were used in a one-pot coprecipitation synthesis. Notable in the present results is the lack of a sextet component associated with Fe_2O_3. Since the hyperfine Mössbauer parameters of Fe^{3+} in weakly ferromagnetic spin states related to Fe_2O_3 [39] differ from those associated with the aforementioned spinel phase, Mössbauer spectroscopy has hereby resolved the overlap issue between γ-Fe_2O_3 and $NiFe_2O_4$ in favor of the last, in line with the LCF analysis of the Fe K edge XANES data.

Summarizing, TMS indicates – in good approximation to LCF analysis of the Fe K edge XANES spectrum – that ~33–41% of Fe in the as prepared sample is present as a $NiFe_2O_4$ spinel phase, which orders magnetically, and ~59–67% as an Fe^{3+}-substituted $MgAl_2O_4$ spinel phase. Based on prior results [22], this latter phase will hereafter be referred to as $MgFe^{3+}{}_xAl_{2-x}O_4$.

To evaluate potential differences between surface and bulk properties of Fe in the catalyst's as prepared state, ILEEMS was performed (Fig. 2B). The spectrum shows a weak emission of only ca. 2%, most likely with a doublet fine structure. Due to the poor statistics, the presence of a magnetic phase could not be verified and the spectrum was analyzed using one single doublet, yielding parameter values as listed in Table 1. The center shift of 0.33 mm/s indicates the valence state of Fe to be Fe^{3+}. Taking into account the center shift and quadrupole splitting values and considering the broad line width, the doublet can actually be composed of two major components arising from Fe^{3+} that substitutes in the octahedral and tetrahedral sites in the $MgAl_2O_4$ spinel phase. While $NiFe_2O_4$ is reported as a bulk phase, an associated sextet component cannot be distinguished in ILEEMS.

In summary, Mössbauer spectroscopy indicates an Fe oxidation state of Fe^{3+} in the catalyst's as prepared state, corroborating XAS results. As Mössbauer spectroscopy identifies only $MgFe_xAl_{2-x}O_4$ and $NiFe_2O_4$, but does not discern Fe_2O_3, this relieves the ambiguity of XRD [20]. More so, the confirmed presence of $NiFe_2O_4$ can account for the observed discrepancies between the as prepared catalyst's XAS spectra and the references in Fig. 1. Further, this identifies Ni present as $NiFe_2O_4$, at least partially, as the molar Ni/Fe ratio in 8Ni5Fe/$MgAl_2O_4$ exceeds 1/2. Hence, the additional presence of NiO and/or $NiAl_2O_4$ must be considered. A schematic representation of the as prepared catalyst state is given in Fig. 3.

3.2. Speciation during and after H_2-TPR

3.2.1. In situ QXAS

Fig. 4 reports the XANES region of the QXAS spectra recorded during H_2-TPR at the Fe K and Ni K edge. Reduction takes place for both Fe and Ni atoms, as evidenced by the decrease in WL intensity, an edge shift to lower energies and an increase of the pre-edge peak intensity.

Inspection of the catalyst's final Fe K and Ni K edge spectra reveals that these do not fully correspond with the associated metallic reference spectra. In part, this can be attributed to the final high temperature,

Table 1
Mössbauer parameters of the Fe^{3+} doublet (D1) fitted to the ILEEMS recorded at RT of as prepared 8Ni5Fe/$MgAl_2O_4$ [a].

Component		δ (mm s^{-1})	ΔE_Q (mm s^{-1})	Γ (mm s^{-1})
D1	Fe^{3+}	0.33(2)	0.89(4)	0.99(4)

[a] δ: center shift (relative to α-Fe at 20 °C); ΔE_Q: quadrupole splitting; Γ:full line width at half maximum.

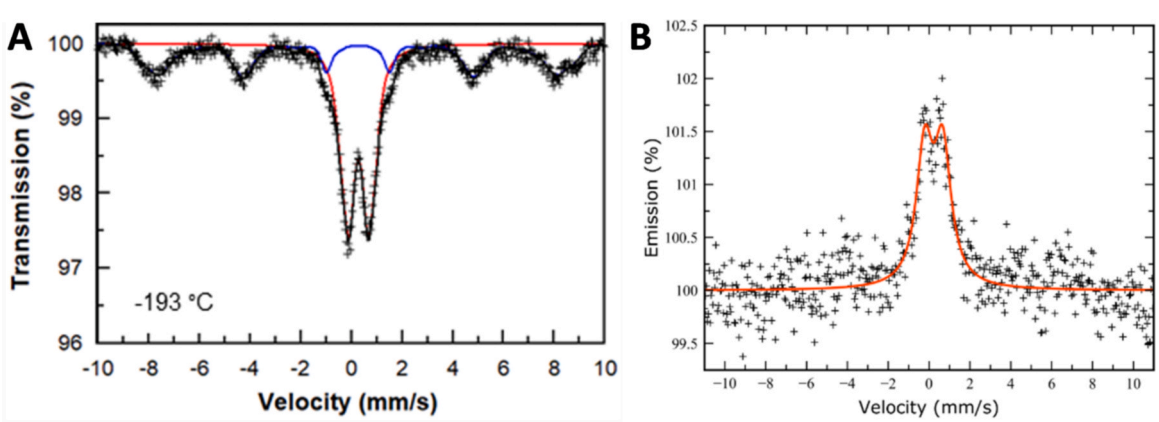

Fig. 2. A: Transmission Mössbauer spectra of as prepared 8Ni5Fe/$MgAl_2O_4$ recorded at −193 °C. + : experimental data; black solid line: spectrum fit; blue solid line: S1 sextet sub-spectrum ((Ni-Fe)-rich spinel phase); red solid line: D1 doublet sub-spectrum (Fe^{3+}-substituted $MgAl_2O_4$ spinel in octahedral and tetrahedral positions). B: ILEEMS of as prepared 8Ni5Fe/$MgAl_2O_4$ at room temperature. + : experimental data; red solid line: spectrum fit, coinciding with the D1 doublet spectrum (Fe^{3+}-substituted $MgAl_2O_4$ spinel in octahedral and tetrahedral positions).

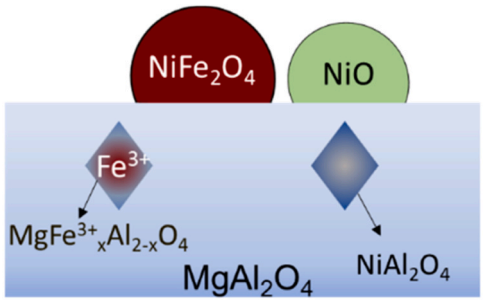

Fig. 3. Schematic representation of the Fe components, as confirmed by Mössbauer spectroscopy, and Ni components, as suggested by XANES, in as prepared 8Ni5Fe/$MgAl_2O_4$.

800 °C, which entails damping of the features beyond the edge, and to the fact that Ni and Fe species are present within the sample as supported nanoparticles [20,22,40,41], which differ in properties from the 'bulk' powder reference species. Furthermore, while it is evident that reduction does occur at both edges, it is plausible that it remains incomplete. Prior XRD measurements in reduced state [20] evidenced the formation of a Ni-Fe alloy phase, next to the support phase. On the other hand, an Fe-modified support $MgFe_xAl_{2-x}O_4$ such as identified by Mössbauer spectroscopy, was found to reduce partially by H_2-TPR [22, 23]. At the Ni K edge, it is likely that there is still some residual oxidized Ni at the end of reduction. As the metals are supported on an oxide, the presence of a $Ni^{\delta+}$ phase, which ensures strong metal-support interactions [22,42] (SMSI), is plausible. SMSI have been reported for different $MgAl_2O_4$-supported Ni catalysts [43–46], along with Ni-Fe systems [22]. In these cases, SMSI were hypothesized to form a Ni-O bond between the Ni-Fe alloy particle and the support, which remained present after H_2-TPR. On the other hand, the presence of a $NiAl_2O_4$ phase, remaining stable under the imposed TPR conditions, cannot be excluded either [20].

To differentiate the components in the catalyst during H_2-TPR, PCA and MCR-ALS were applied to the in situ XAS datasets. Applying PCA to the Fe K edge H_2-TPR dataset detects 3 principal components (PCs) (Fig. S7), while 2 PCs are detected for the Ni K edge (Fig. S8). The component spectra and concentration profiles derived by the MCR-ALS methodology are presented in Fig. 5. Associated goodness of fit parameters are provided in Table S1.

On the Fe K edge dataset (Fig. 5A), MCR-ALS allows extracting spectra of 3 different components, with a starting component which decreases in concentration at ~280 °C, a final component which starts to form at a similar temperature and an intermediate which is maximum at about 620 °C with ca. 40% concentration. Considering the known initial (from Mössbauer spectroscopy) and final [20,22,40] states of Fe within the sample, 4 different components are at play during H_2-TPR: $NiFe_2O_4$, $MgFe^{3+}{}_xAl_{2-x}O_4$, its reduced counterpart $MgFe^{2+}{}_xAl_{2-x}O_4$ [22] together with Ni-Fe alloy [22,40,41,47]. However, the MCR-ALS profile detects only one component at the start of reduction. This is caused by the fact that MCR-ALS can only distinguish species that evolve via different routes, yielding a different variance profile [48]. As a consequence, the Fe component derived by MCR-ALS is actually a 'merged' version of multiple Fe phases with different physicochemical nature, in this case $NiFe_2O_4$ and $MgFe^{3+}{}_xAl_{2-x}O_4$, which evolve similarly during TPR [24,49]. By MCR-ALS, they will be "merged" into one combi-phase with a spectrum corresponding to a mixture of the two. A one-on-one identification of the derived Fe K edge component spectra is therefore not possible from XAS data alone. At the end of TPR, still under H_2 at 800 °C, a single component appears to be present, with a XANES spectrum resembling the one of metal Fe, which might hence be linked to the Ni-Fe alloy. As for the intermediate state, appearing from 280 °C onwards, this could well originate from Fe^{2+} species, both in the support $MgFe_xAl_{2-x}O_4$ and as intermediate in partially reduced $NiFe_2O_4$.

For the Ni K edge dataset, only two components are deduced (Fig. 5B), corresponding to the initial and final state of the catalyst in the experiment. Herein, a slow change in the compositional fractions precedes a noticeable steep increase/decrease starting at ~500 °C. Given the fact that the former change is rather small in comparison to the latter and the fact that the slow rise occurs from the start of the TPR profile onwards, it is probable that these are the result of a temperature effect rather than a change in chemical nature, i.e. reduction, of the Ni species. Above 500 °C, this temperature effect is still present, yet is now dominated by actual reduction of Ni species. A similar observation, though less obvious, can be made for the Fe species, where a weak slope is noticed in the concentration profiles for the Fe components below 280 °C. In view of the as prepared state's characterization results, component 1 corresponds to a superposition of Ni species in $NiFe_2O_4$ and NiO. For component 2, metallic Ni is likely the dominant contribution. An SMSI-related NiO phase contribution could persist but possibly in too small a concentration to be detectable. Additionally, as this method relies on variation in the data, it cannot be excluded that a $NiAl_2O_4$ phase, invariant below 900 °C [50], is equally present but goes unnoticed by MCR-ALS in this reduction process. Numerical experiments (Fig. S9) confirmed that the presence of a small amount (< 10%) of $NiAl_2O_4$ indeed cannot be excluded.

3.2.2. *Mössbauer spectroscopy – reduced*

To further assess the identity of Fe species in the reduced sample, ex situ TMS were recorded at RT after reduction, as shown in Fig. 6A. The spectrum is adequately described by a superposition of two Lorentzian-

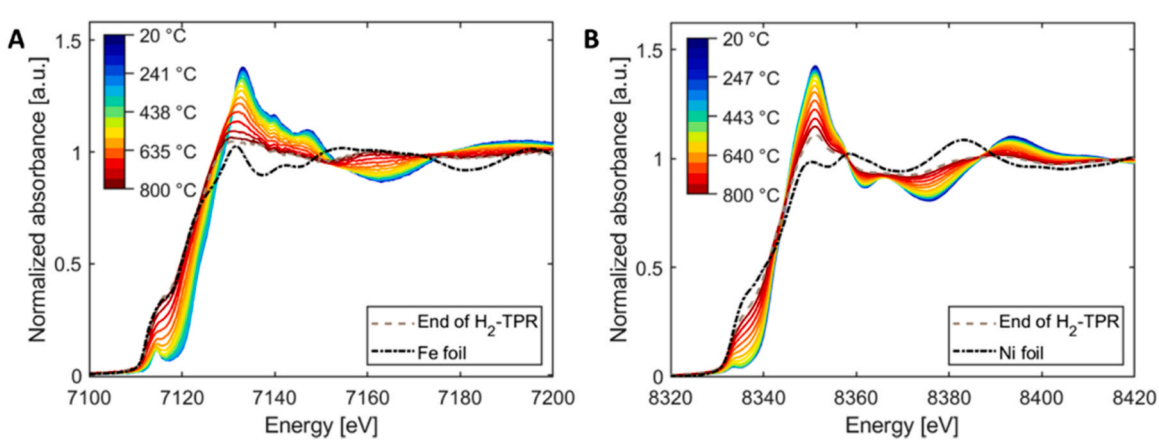

Fig. 4. In situ QXANES spectra recorded during H_2-TPR (10 °C/min, up to 800 °C, for 30 min) of as prepared 8Ni5Fe/$MgAl_2O_4$ at (A) the Fe K edge and (B) the Ni K edge.

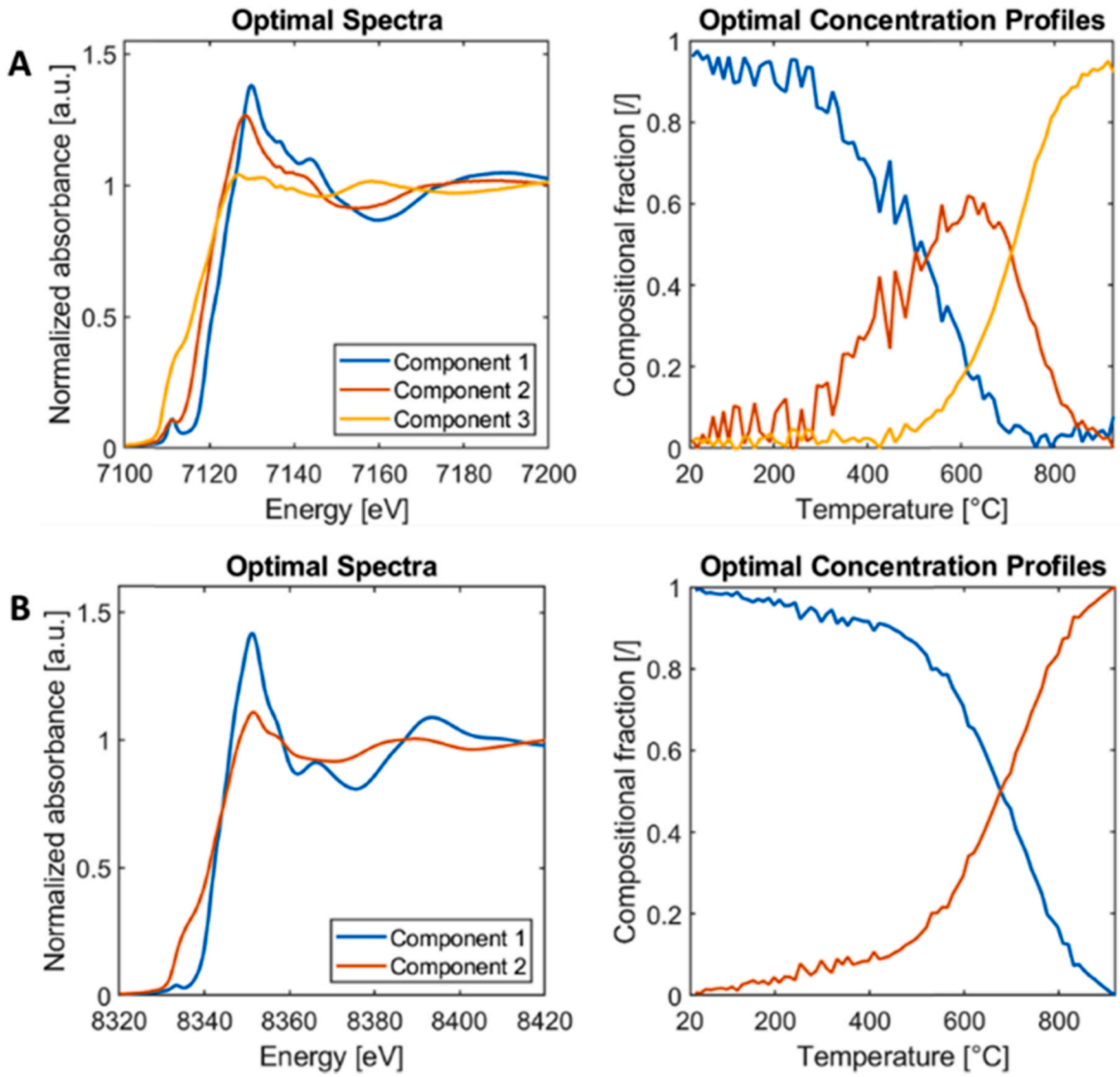

Fig. 5. MCR-ALS results for in situ QXAS data recorded at (A) the Fe K edge and (B) Ni K edge during H_2-TPR (10 °C/min, up to 800 °C, for 30 min) of as prepared 8Ni5Fe/$MgAl_2O_4$. The component spectra are limited to the XANES region for ease of interpretation.

shaped sextets (S1 and S2), an Fe^{3+} quadrupole doublet (D1) and an Fe^{2+} quadrupole doublet (D2). The adjusted parameter values are listed in Table 2.

The values of the hyperfine parameters for S1 and S2 suggest that both sextets are due to two Ni-Fe alloy phases with different Ni/Fe composition [51]. This is plausible considering the nature of the freshly

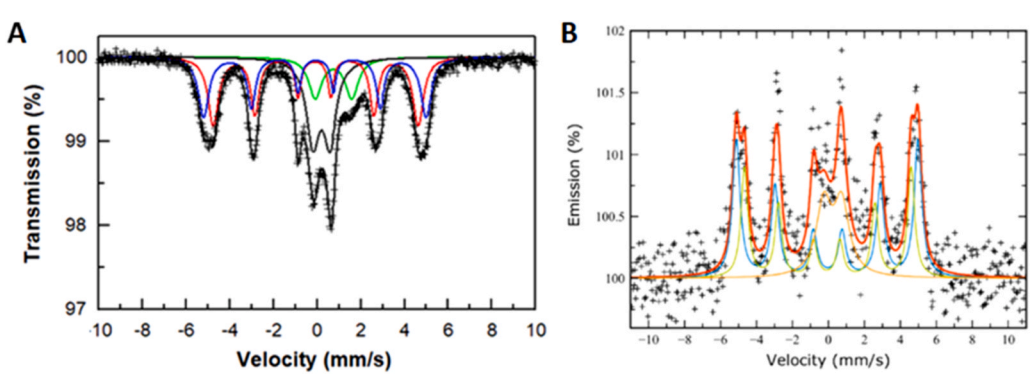

Fig. 6. A: Transmission Mössbauer spectra of reduced 8Ni5Fe/$MgAl_2O_4$ recorded at RT. +: experimental data; black solid line: spectrum fit; red solid line: S1 sextet sub-spectrum (Ni-Fe alloy with low at% Ni); blue solid line: S2 sextet sub-spectrum (Ni-Fe alloy with high at% Ni); black solid line: D1 doublet sub-spectrum (Fe^{3+}-substituted $MgAl_2O_4$ spinel in octahedral and tetrahedral positions); black solid line: D2 doublet sub-spectrum (Fe^{2+}-substituted $MgAl_2O_4$ spinel in octahedral and tetrahedral positions). B: Experimental (+) and calculated (red solid line) ILEEMS of reduced 8Ni5Fe/$MgAl_2O_4$ recorded at RT. +: experimental data; red solid line: spectrum fit; blue solid line: S1 sextet sub-spectrum (Ni-Fe alloy with low at% Ni); green solid line: S2 sextet sub-spectrum (Ni-Fe alloy with high at% Ni); orange solid line: D1 doublet sub-spectrum (Fe^{3+}-substituted $MgAl_2O_4$ spinel in octahedral and tetrahedral positions).

Table 2
Mössbauer parameters of the two sextets (S1 and S2), the Fe^{3+} doublet (D1) and Fe^{2+} doublet (D2) fitted to the TMS of reduced 8Ni5Fe/$MgAl_2O_4$ at RT.[a].

Component		H_{hf} (kOe)	$2\varepsilon_Q$ (mm s^{-1})	δ (mm s^{-1})	ΔE_Q (mm s^{-1})	RA (%)
S1	Fe^0	315	-0.05	0.04		29
S2	Fe^0	291	0.06	0.02		33
D1	Fe^{3+}			0.31	0.78	25
D2	Fe^{2+}			0.88	1.68	12

[a] In case of distributions, the parameters mentioned are those with the highest probability. H_{hf}: magnetic hyperfine field; $2\varepsilon_Q$: quadrupole shift; δ: center shift (relative to α-Fe at 20 °C); ΔE_Q: quadrupole splitting; RA: relative area.

prepared parent oxide phases and the broad compositional range of the Ni-Fe alloy as indicated by the Ni-Fe system phase diagram [52]. Johnson et al. [53] reported hyperfine fields gradually varying at RT from ~300 kOe to ~280 kOe upon increasing the at% Ni from 35 to more than 90. According to these results, S1 would arise from a Ni-Fe alloy with relatively low at% Ni, and S2 from a Ni-Fe alloy with higher at% Ni. However, whether it really concerns two distinct alloys is not irrefutable; the two resolved sextets might actually represent a first approximation for the existence of Ni-Fe alloy with a broad range for the Ni/Fe ratio. Attempts to fit the six-line component using a HFD yielded goodness-of-fit values that were significantly higher than for the model using two discrete sextets.

The presence of both an Fe^{2+} and Fe^{3+} quadrupole doublet in the reduced sample, linked to the Fe-modified support $MgFe_xAl_{2-x}O_4$, is in line with previous findings from QXAS measurements [22]. The line widths for the fitted ferrous and ferric doublets are quite broad, i.e., $\Gamma \approx 0.75$ mm/s, compared to ~0.27 mm/s for standard α-Fe at RT, suggesting that both resolved doublets are each composed of at least two major contributions. Likely, these two would arise from octahedral and tetrahedral Fe^{2+} and Fe^{3+}, respectively, in the parent spinel. Note that the adjusted values of δ and ΔE_Q are in line with those obtained for the doublet found for the freshly prepared oxide.

The ILEEMS of the reduced catalyst is reproduced in Fig. 6B. Again, a weak emission of ca. 1.5% is detected. However, the appearance of a six line pattern is obvious, indicating the presence of some magnetic ordering in the particles' surface layers. The spectrum was analyzed using two sextets (S1 and S2, both with imposed line area ratios of 3:2:1 for outer to middle to inner emission lines) and one symmetric Fe^{3+} quadrupole doublet (D). The adjusted Mössbauer parameters are given in Table 3. The sextet parameters are close to those obtained from TMS using a similar fitting model, indicative of Ni-Fe alloys with a broad range for the Ni/Fe ratio at the reduced sample's surface [53]. Taking into account the poor statistics, the doublet parameters probably suggest that the resolved doublet, like for the as prepared sample, is also composed of at least two major components, possibly arising from octahedral and tetrahedral Fe^{3+} in the spinel phase. While an

Table 3
Mössbauer parameters of the two sextets (S1 and S2) and the Fe^{3+} doublet (D1) fitted to the ILEEMS of reduced 8Ni5Fe/$MgAl_2O_4$ at RT.[a].

Component		H_{hf} (kOe)	$2\varepsilon_Q$ (mm s^{-1})	δ mm s^{-1})	ΔE_Q (mm s^{-1})	Γ (mm s^{-1})	RA (%)
S1	Fe^0	313(1)	-0.03 (1)	0.053 (9)		0.51 (5)	45
S2	Fe^0	287(1)	0.06(3)	0.04 (1)		0.47 (4)	32
D	Fe^{3+}			0.35 (4)	0.99(6)	1.0(1)	23

[a] In case of distributions, the parameters mentioned are those with the highest probability. H_{hf}: magnetic hyperfine field; $2\varepsilon_Q$: quadrupole shift; δ center shift (relative to α-Fe at RT); ΔE_Q: quadrupole splitting; Γ: full line width at half maximum; RA: relative area.

Fe^{2+}-substituted $MgAl_2O_4$ spinel is not resolved, it is possible that, given the small RA value in TMS, an associated contribution in ILEEMS is overwhelmed by noise.

It can be concluded that both the surface and bulk Fe species of the reduced sample comprise similar components: a Ni-Fe alloy with a broad range for the Ni/Fe ratio and the Fe-substituted $MgFe_xAl_{2-x}O_4$ spinel phase, with both Fe^{3+} and Fe^{2+} presence. Comparison of the RA values of TMS and ILEEMS reveals that the contributions of the alloys are higher for ILEEMS than for TMS. This can be explained through the fact that Ni-Fe alloys are mainly created through the reduction of surface $NiFe_2O_4$ species by exposure to the reducing environment. As such, the surface is enriched in alloy phase, which leads to relatively higher RA values when analyzing the sample with surface-sensitive techniques. Additionally, the co-existence of Fe^{2+}- and Fe^{3+}-substituted $MgAl_2O_4$ support phases is discerned in the reduced catalyst. This is in line with the partial reduction of $MgFe^{3+}{}_xAl_{2-x}O_4$ into $MgFe^{2+}{}_xAl_{2-x}O_4$ [22–24].

3.2.3. Discussion

The TMS and ILEEMS results of both the as prepared and reduced samples suggest the presence of different Fe species throughout H_2-TPR of an as prepared 8Ni5Fe/$MgAl_2O_4$ catalyst. At the start, $NiFe_2O_4$ and $MgFe^{3+}{}_xAl_{2-x}O_4$ are present, while $MgFe^{2+}{}_xAl_{2-x}O_4$, and Ni-Fe alloy (with a dual distribution of high and low Ni/Fe ratios) are discerned after completion of the reduction experiment. From its absence in XRD [20] and Mössbauer spectra in the reduced state, it is evident that $NiFe_2O_4$ reduces completely into a Ni-Fe alloy. However, reported reduction mechanisms for the aforementioned spinel vary with its preparation method. Benrabaa et al. [54] examined $NiFe_2O_4$ prepared by two methods: co-precipitation and hydrothermal synthesis. When subjected to H_2-TPR, both types of $NiFe_2O_4$ displayed a reduction mechanism consisting of consecutive reduction of Ni and Fe:

$$NiFe_2O_4 \rightarrow Ni + Fe_2O_3 \quad (20 - 375\,^\circ C) \tag{2}$$

$$Fe_2O_3 + Ni \rightarrow Fe_xNi_y \quad (375 - 600\,^\circ C) \tag{3}$$

Chamoumi and co-workers [55] investigated samples synthesized by solid-state reaction. A mechanism was proposed wherein $NiFe_2O_4$ is first reduced to Ni and FeO at ~460 °C, followed by a final reduction step of FeO to metallic Fe, which then forms a Ni-Fe alloy upon interaction with metallic Ni. In the work of Zhang et al. [56], the decomposition of $NiFe_2O_4$ into NiO and Fe_3O_4 is reported, followed by a subsequent reduction of these subcomponents. The reduction mechanism they proposed in the range 300 – 550 °C was of the form (with increasing temperature):

$$NiFe_2O_4 \rightarrow NiO + Fe_3O_4 \rightarrow Fe_3O_4 + Ni \rightarrow FeO + Fe_xNi_y \rightarrow Fe_xNi_y + Fe \tag{4}$$

Investigations of $NiFe_2O_4$ supported on $CeZrO_2$ were performed by Dharanipragada et al. [57]. Herein, in situ XRD during H_2-TPR shows no NiO or Fe oxide, suggesting that $NiFe_2O_4$ is directly reduced to metallic Fe and Ni in the temperature range 200 – 700 °C. Ma et al. [49] also investigated $NiFe_2O_4$ supported on $CeZrO_2$, ZrO_2 and CeO_2, and concluded that all samples reduce similarly in the temperature range of 200 – 900 °C. In contrast to Dharanipragada et al. [57], they proposed a mechanism of the form $NiFe_2O_4 \rightarrow Ni + Fe_3O_4 \rightarrow NiFe$.

The present in situ QXAS data indicate an onset of reduction at temperatures that are lower for Fe species (~280 °C) than for Ni species (~500 °C). Considering the MCR-ALS results at both edges, no formal identification of any of the abovementioned reduction mechanisms is possible. While it is conceivable that the second component derived from the Fe K edge data stems from an intermediate - as implied by its concentration profile, e.g. Fe_3O_4 or FeO -, the merging of components with equal evolution prevents a one-on-one physicochemical identification. In addition and concomitant to $NiFe_2O_4$ reduction [49], partial reduction of $MgFe^{3+}{}_xAl_{2-x}O_4$ to $MgFe^{2+}{}_xAl_{2-x}O_4$ takes place [22–24], as evidenced by TMS. However, the relative presence of Fe in $MgFe^{3+}{}_xAl_{2-x}O_4$ changes upon reduction: from 59% to 67% for the as

prepared catalyst to roughly 37% for the combination of $MgFe^{3+}{}_xAl_{2-x}O_4$ and $MgFe^{2+}{}_xAl_{2-x}O_4$ according to the TMS analysis. Indeed, it has been reported [22] that H_2-TPR can induce hydrogen spillover from the reduced catalyst's surface species onto the support, thus enabling the migration of support Fe to the surface alloy phase [22]. The migration of Fe from $MgFe_xAl_{2-x}O_4$ during reduction has also been confirmed by Longo et al. [58]. On the basis of Rietveld refinement, they found that ~12% of $MgFeAlO_4$ segregated as $MgFeO_x$, while the remaining part of the $MgFeAlO_4$ spinel phase was retained, albeit with partial reduction of Fe^{3+} to Fe^{2+}. It is thus possible that this $MgFeO_x$ phase also forms during reduction of 8Ni5Fe/$MgAl_2O_4$, as a precursor for Fe migrating out of the support.

The partially reduced support goes unnoticed in the MCR-ALS analysis of the in situ QXAS data. The latter could be due to the involved Fe fractions being smaller than the ones from Ni-Fe alloy, roughly 1/3 for the combination of $MgFe^{3+}{}_xAl_{2-x}O_4$ and $MgFe^{2+}{}_xAl_{2-x}O_4$ based on the TMS analysis. Then again, since TMS was performed ex situ, it is equally possible that the actual Fe fractions in the support during high temperature reduction are even lower, in favor of the NiFe alloy fraction. Hence, two Fe contributions can be considered for Ni-Fe alloy formation: $NiFe_2O_4$ reduction as main alloy source and possibly migration of Fe out of $MgFe_xAl_{2-x}O_4$ towards reduced Ni.

For the Ni species, the $NiFe_2O_4$ phase is accompanied by NiO, which both reduce to a metallic Ni state, incorporated into Ni-Fe alloy. H_2-TPR studies on Ni/$MgAl_2O_4$ indicate that supported NiO starts to reduce at 450–500 °C [59–61], which is in agreement with the concentration profiles derived by MCR-ALS for the Ni K edge spectra (Fig. 5B). Previously, an in situ XRD study of the present 8Ni5Fe/$MgAl_2O_4$ catalyst found NiO to reduce at ~500 °C, after which alloying with Fe took place. The fact that $NiFe_2O_4$ and NiO are not differentiated by MCR-ALS further strengthens the hypothesis that the steep increase in the compositional fraction of the Ni components corresponds to the joined reduction of $NiFe_2O_4$-related Ni species and NiO. In addition, a stable $NiAl_2O_4$ contribution cannot be excluded.

Summarizing, the results indicate a reduction mechanism as represented in Fig. 7. Herein, the reduction of Fe species in $NiFe_2O_4$ and $MgFe^{3+}{}_xAl_{2-x}O_4$ can be considered to occur quasi-simultaneously. $NiFe_2O_4$ reduces completely to Ni-Fe alloy via a mechanism that is as of yet unknown, while $MgFe^{3+}{}_xAl_{2-x}O_4$ reduces partially to $MgFe^{2+}{}_xAl_{2-x}O_4$. A related migration of Fe to the catalyst surface, which contributes to the alloy formation, is not excluded. Reduction of Ni in $NiFe_2O_4$ and NiO from 500 °C on leads to the formation of Ni^0, which is embedded in the Ni-Fe alloy. A final, residual fraction of oxidic Ni in SMSI-related Ni – O bonds is plausible, while a small (< 10%) Ni fraction related to invariant $NiAl_2O_4$ is equally likely.

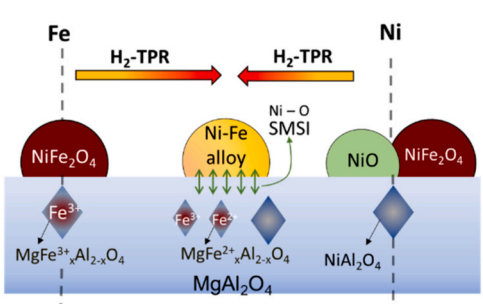

Fig. 7. Schematic representation of the reduction mechanism of as prepared 8Ni5Fe/$MgAl_2O_4$ via H_2-TPR (10 °C/min, up to 800 °C, for 30 min), based on QXAS with MCR-ALS analysis and Mössbauer spectroscopy. Dashed grey lines: as prepared state; ↔: SMSI.

3.3. Speciation during and after DRM

3.3.1. In situ QXAS

The current 8Ni5Fe/$MgAl_2O_4$ catalyst achieves in DRM with feed ratio 1/1 a CH_4 conversion of 35% after 4 h TOS and a CO/H_2 ratio of 1.35, as has been reported previously [20]. The present study focuses on linking the behavior of the Ni and Fe species in this catalyst under DRM conditions with this performance. The Fe K edge QXAS spectra recorded during consecutive DRM experiments on a reduced or regenerated catalyst for different CH_4/CO_2 ratios R_c are presented in Fig. 8. The initial Fe K spectra are quasi-identical for all experiments, indicating that post-reaction H_2 reduction can regenerate the catalyst. From the evolution of the edge position and WL intensity, it is clear that oxidation of the Fe species occurs for $R_c < 1/1$. When $R_c = 1/2$, the oxidation appears to be stronger than for $R_c = 1/1.5$, as a higher final WL intensity is observed in the former case, 1.17 vs. 1.15. At $R_c = 1/1$, no net oxidation takes place, although fluctuations in the Fe K edge position occur which are on the order of ~0.3–0.6 eV. For all R_c values, the recorded Ni K edge spectra (Fig. S10) display no net oxidation and are quasi-similar. Yet again, fluctuations appear in the edge position that are on the order of ~0.3–0.6 eV.

PCA analysis of these data discerns 2 PCs at the Fe K edge for $R_c = 1/2$ (Fig. S11) and 1/1.5 (Fig. S12), while only 1 is derived for $R_c = 1/1$ (Fig. S13). For all corresponding Ni K edge datasets, 1 PC is derived (Figs. S14, S15 and S16), confirming the invariant Ni state. MCR-ALS analysis is thus limited to the $R_c = 1/2$ and 1/1.5 Fe K data and leads for both datasets to the derivation of identical components (Fig. 9). The corresponding goodness of fit parameters are provided in Table S2.

The first component was identified at the end of reduction as being mainly Ni-Fe, whether or not merged from different alloy compositions, with a possible unresolved contribution from $Fe^{2+/3+}$-containing $MgAl_2O_4$. During 30 min of DRM, the XAS spectrum for $R_c = 1/2$ and $R_c = 1/1.5$ evolves versus a 60:40 and 90:10 distribution, respectively, between this original reduced component 1 and a component 2, for which a merging effect again cannot be excluded. Based on the WL intensities and pre-edge features of the derived spectral components, it follows that component 2 bears a more oxidized signature. A comparison with reference spectra (Fig. S17) corroborates this, as the component's edge is positioned between those of FeO and Fe_3O_4. However, its pre-edge feature bears little resemblance to those of oxide references.

Prior in situ XRD experiments for 8Ni5Fe/$MgAl_2O_4$ have elucidated the formation of FeO in DRM under larger CO_2 partial pressures, i.e. $R_c = 1/6$ [20]. For lower values of R_c, this phase was not seen in XRD, which however does not exclude its presence in small concentrations or as crystallites too small to be detected by XRD. XAS, however, is able to detect such oxidized Fe phase even for lower CO_2 concentrations in the feed. This is consistent with the operando XAS results of Kim and co-workers [19], who observed Fe oxide formation during DRM of Ni-Fe/$Mg_xAl_yO_z$. However, for $R_c = 1/1$, they confirmed FeO formation while the present XAS results do not. This can be related to the $MgAl_2O_4$ spinel support used in the current study, which is in contrast to the hydrotalcite-derived $Mg_xAl_yO_z$ material employed by Kim et al. [19]. Upon exposure to DRM gases with $R_c < 1/1$, CO_2 indeed induces a net oxidation effect in the Fe species. This oxidation takes place only to a certain extent and within the first ~5–10 min, indicating that the Fe species within the catalyst attain a new steady-state composition under the imposed DRM conditions. Higher steady-state oxide weights are derived for lower R_c values, indicating a more advanced oxidation at higher CO_2 concentrations.

As no noticeable changes are noticed for all the Ni K edge datasets as well as for the $R_c = 1/1$ Fe K edge dataset, it is concluded that these activated catalyst's species don't change significantly under the associated conditions.

3.3.2. Mössbauer spectroscopy – DRM, $R_c = 1/2$

To further identify the Fe species, TMS was performed on an

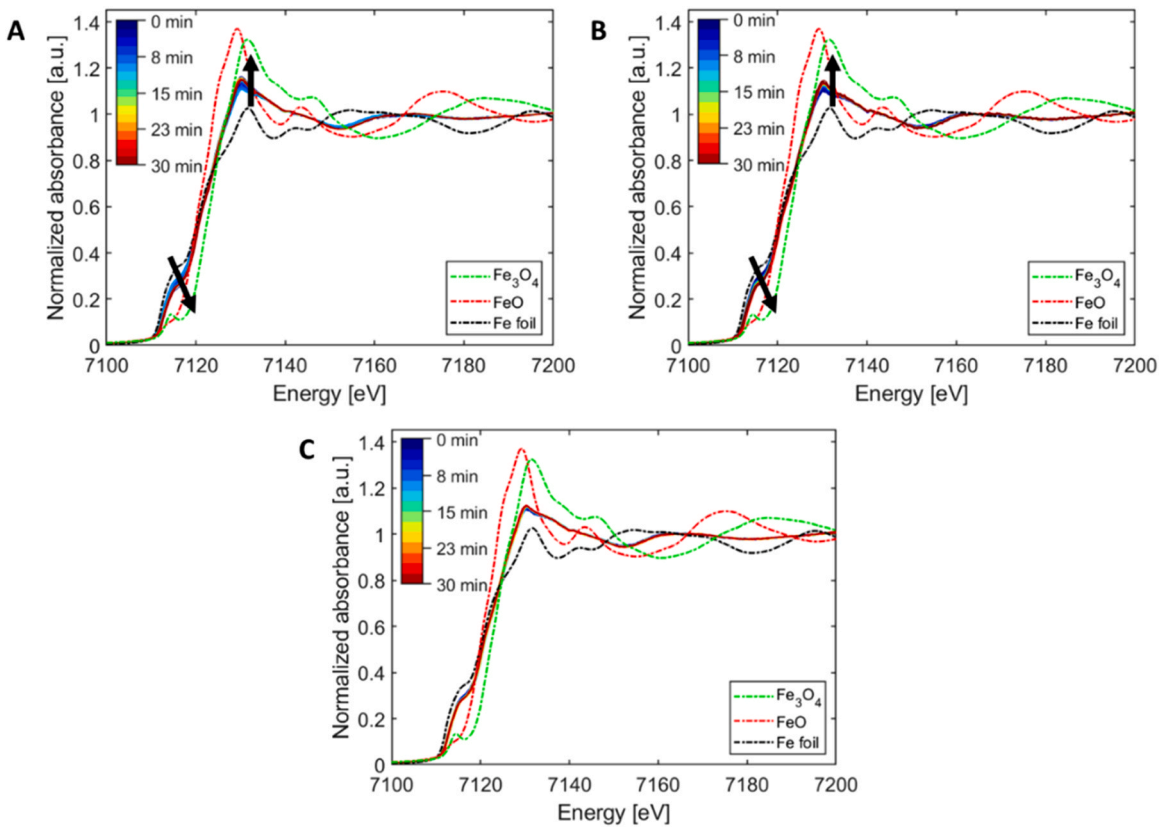

Fig. 8. In situ Fe K edge QXANES spectra recorded during DRM (750 °C, 1 atm, 30 min) of reduced 8Ni5Fe/$MgAl_2O_4$ with CH_4/CO_2 = (A) 1/2, (B) 1/1.5 and (C) 1/1. Solid lines: experimental spectra; dashed lines: reference spectra; bold arrows: evolution of the spectra during DRM.

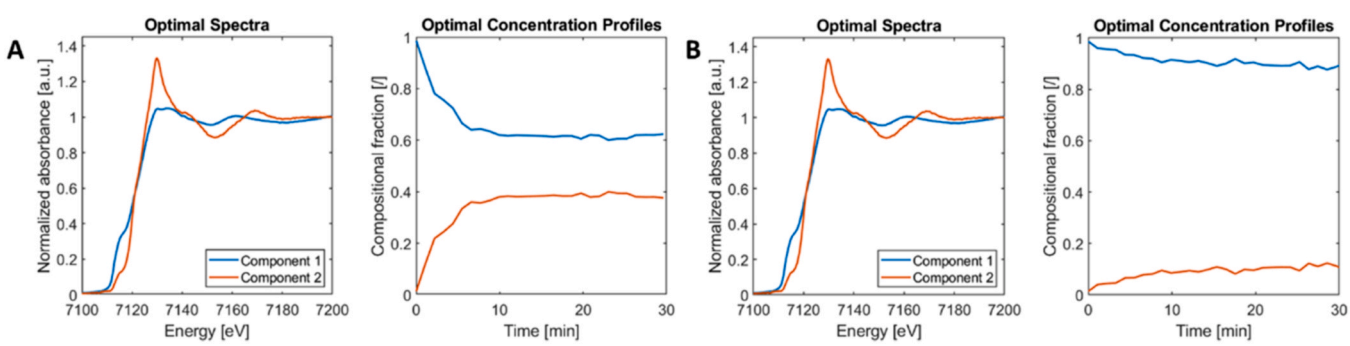

Fig. 9. MCR-ALS results for in situ QXAS data recorded at the Fe K edge during DRM (750 °C, 1 atm, 30 min) with CH_4/CO_2 = (A) 1/2 and (B) 1/1.5 of reduced 8Ni5Fe/$MgAl_2O_4$. The component spectra are limited to the XANES region for ease of interpretation.

activated sample exposed to DRM conditions with $R_c = 1/2$ (Fig. S18). The spectrum is similar to that recorded for the reduced sample, and is therefore fitted using the same superposition of two sextets (S1 and S2) and two doublets (D1 and D2). The adjusted Mössbauer parameters are collected in Table 4. Compared to TMS for the reduced sample, small differences in terms of RA values are discerned, with a slight increase for the doublet contribution. The latter could point to reincorporation of some Fe into the support lattice. The presence of an additional FeO phase is not resolved, though it is possible that its spectral features are masked in the broadly distributed doublet components [62].

3.3.3. Mössbauer spectroscopy – DRM, $R_c = 1/1$

TMS was also performed for a reduced catalyst exposed to DRM gases with $R_c = 1/1$ to investigate the Fe species under these conditions. The results are provided in Fig. S19. This spectrum is again similar in shape to those of the reduced and DRM-used sample at higher CO_2 partial

Table 4
Mössbauer parameters of the two sextets (S1 and S2), the Fe^{3+} doublet (D1) and Fe^{2+} doublet (D2) fitted to the TMS of 8Ni5Fe/$MgAl_2O_4$ recorded at RT after DRM (750 °C, 1 atm, 30 min) with CH_4/CO_2 = 1/2.[a].

Component		H_{hf} (kOe)	$2\varepsilon_Q$ (mm s^{-1})	δ (mmσ^{-1})	ΔE_Q (mm s^{-1})	RA (%)
S1	Fe^0	315	-0.05	0.03		24
S2	Fe^0	289	0.07	0.02		34
D1	Fe^{3+}			0.33	0.75	28
D2	Fe^{2+}			0.83	1.75	14

[a] In case of distributions, the parameters mentioned are those with the highest probability. H_{hf}: magnetic hyperfine field; $2\varepsilon_Q$: quadrupole shift; δ: center shift (relative to α-Fe at 20 °C); ΔE_Q: quadrupole splitting; RA: relative area.

pressure. Consequently, the spectrum was modelled in the same way and the adjusted parameter values are reported in Table 5.

Within experimental error limits, the hyperfine parameters of the Fe phases in this sample are the same as those of the reduced and the DRM-used sample with non-equimolar gas concentrations. This instigates that the type of phases has not been altered by the prolonged DRM treatment. Nevertheless, marked changes in the RA values are noticeable: these have decreased for both Fe^{2+} and Fe^{3+} doublets in favor of the Ni-Fe alloy sextet components, while keeping the same ratio of Fe^{2+} to Fe^{3+}, i.e. 1:2.

An ILEEMS was also recorded under the same conditions (Fig. 10). As before, the emission is low and the statistics are quite poor. Nevertheless, the appearance of a six line pattern is recognized, indicating that some magnetic ordering occurs in the surface layers of the sample's particles. Contrary to ILEEMS of the reduced sample, only one sextet S could be resolved. In addition, the presence of significant emission centered around zero velocity was apparent and fitted as one symmetric Fe^{3+} quadrupole doublet D.

The relevant adjusted Mössbauer parameters are given in Table 6. Based on the parameter values, it is not feasible to infer correlation between sextets S1 and S2 of the reduced sample and sextet S of this DRM-used sample. Sextet S shows a very broad line width (~0.9 mm/s), which is possibly due to Ni-Fe alloys with a broad distribution for the Ni/Fe ratio [53], so this could still match the 2 sextets that were resolved in ILEEMS for the reduced sample (Fig. 6B).

Roughly, the doublet parameters are in accordance with the results obtained for the reduced sample, and the doublet can therefore again be attributed to octahedral and tetrahedral Fe^{3+} in the spinel phase. As before, an Fe^{2+}-substituted $MgAl_2O_4$ spinel is not resolved. As its RA value in TMS is even smaller than for the reduced sample, 8 vs. 12%, an associated contribution in ILEEMS is not expected to protrude above the noise. Remarkably, the RA values of the doublet are equal for the reduced and the present DRM-used sample, ca. 23%, indicating that the surface composition has not changed after DRM with $R_c = 1/1$.

While the Ni-Fe alloys formed upon reduction are surface species [15,16,20,40,63–65], the increase of the alloy phase's RA with respect to the Fe-modified spinel after DRM is not reflected in ILEEMS, only in TMS. Given the ILEEMS information depth of ~5 nm versus the reported size of 14.3 nm for the alloy particles [20], it is plausible that additional Fe alloying goes unnoticed in ILEEMS. On the other hand, the low data quality of ILEEMS will surely entail higher experimental error, also in the RA values.

3.3.4. Discussion

From the collective analysis of Mössbauer spectroscopy and in situ QXAS, it follows that the compositional changes occurring in the activated catalyst during DRM depend on the applied R_c value. These results can be explained through the following considerations. As found by TMS and MCR-ALS, the activated catalyst consists predominantly of Ni-Fe alloy, along with $MgFe^{2+}{}_xAl_{2-x}O_4$, $MgFe^{3+}{}_xAl_{2-x}O_4$, and potentially $NiAl_2O_4$ and SMSI-related NiO as separate Ni phases. Theofanidis et al. [20] suggest DRM on Ni-Fe/$MgAl_2O_4$ takes place on the alloy via a Mars-van Krevelen mechanism. Herein, the Ni sites activate the dissociation of CH_4, while the alloy's constituent Fe sites are oxidized by CO_2 to FeO_x. The latter is subsequently reverted into Fe through reduction by C, CH_x and H species, originating from CH_4 dissociation.

With the confirmed presence of Fe in the $MgAl_2O_4$ support, this scheme must be extended. Indeed, studies on Ni/$MgFe_xAl_{2-x}O_4$ have substantiated the redox abilities of $MgFe^{Y+}{}_xAl_{2-x}O_4$ (where Y = 2 or 3) species [22,66]; they can oxidize CH_4 dissociation products and can be oxidized by CO_2 and/or H_2O. On its own though, Fe in $MgFe^{Y+}{}_xAl_{2-x}O_4$ is far less active in DRM than supported Ni-Fe/$MgAl_2O_4$ [20,22]. Hence, a Mars-van Krevelen mechanism is proposed which accounts for the contribution of both this Fe-substituted $MgAl_2O_4$ and supported Ni-Fe species, as represented schematically in Fig. 11.

Fig. 12 displays the changes during DRM for different values of R_c. In the case of more oxidizing conditions ($R_c < 1$) (Fig. 12B), the CH_4 dissociation products are less abundant, such that a net oxidation of Fe takes place by the more dominant CO_2. Oxidation of Ni by CO_2 under DRM conditions is unfavorable [20], hence Ni retains its metallic state. According to MCR-ALS of the in situ QXAS data, 40% ($R_c = 1/2$) of Fe gets re-oxidized towards FeO during DRM, leaving 60% in alloyed state. Although the lineshape of component 2 in Fig. 9A confirms an oxidized Fe state, the existence of FeO_x during DRM cannot be confirmed unambiguously with the current results. In comparing with model references, the difference in temperature between the reference (RT) and the catalyst recording (750 °C), and the different nature of the signal

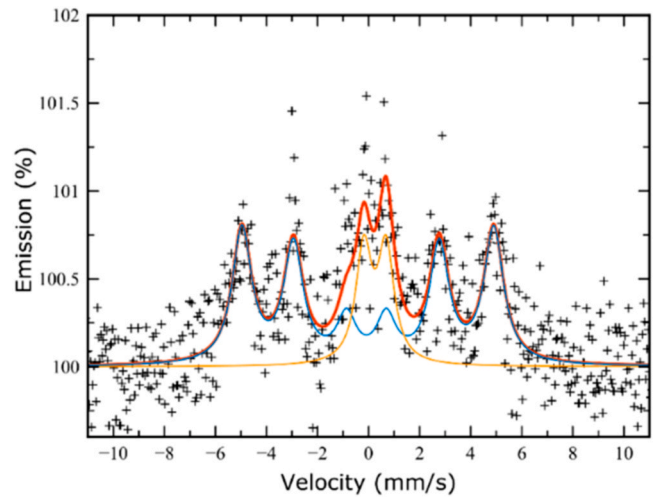

Fig. 10. ILEEMS of 8Ni5Fe/$MgAl_2O_4$ after DRM (750 °C, 1 atm, 30 min) with $CH_4/CO_2 = 1/1$, recorded at RT. + : experimental data; red solid line: spectrum fit; blue solid line: S sub-spectrum (Ni- Fe alloy with broad Ni/Fe range); orange solid line: D doublet sub-spectrum (Fe^{3+}-substituted $MgAl_2O_4$ spinel in octahedral and tetrahedral positions).

Table 5
Mössbauer parameters of two sextets (S1, S2), the Fe^{3+} and Fe^{2+} doublet (D1, D2, respectively) fitted to the TMS of 8Ni5Fe/$MgAl_2O_4$ recorded at RT after DRM (750 °C, 1 atm, 30 min) with $CH_4/CO_2 = 1/1$.[a].

Component		H_{hf} (kOe)	$2\varepsilon_Q$ (mm s^{-1})	δ (mm s^{-1})	ΔE_Q (mm s^{-1})	RA (%)
S1	Fe^0	315	-0.05	0.03		38
S2	Fe^0	291	0.07	0.03		38
D1	Fe^{3+}			0.31	0.7	16
D2	Fe^{2+}			0.85	1.78	8

[a] In case of distributions, the parameters mentioned are those with the highest probability. H_{hf}: magnetic hyperfine field; $2\varepsilon_Q$: quadrupole shift; δ: center shift (relative to α-Fe at 20 °C); ΔE_Q: quadrupole splitting; RA: relative area.

Table 6
Mössbauer parameters of the sextet (S) and the Fe^{3+} doublet (D) fitted to the ILEEMS of 8Ni5Fe/$MgAl_2O_4$ recorded at RT after DRM (750 °C, 1 atm, 30 min) with $CH_4/CO_2 = 1/1$.[a].

Component		H_{hf} (kOe)	$2\varepsilon_Q$ (mm s^{-1})	δ (mm s^{-1})	ΔE_Q (mm s^{-1})	Γ (mm s^{-1})	RA (%)
S	Fe^0	306 (3)	0.06 (5)	0.05 (4)		0.92 (7)	76
D	Fe^{3+}			0.35 (4)	0.87(6)	0.8(1)	24

[a] In case of distributions, the parameters mentioned are those with the highest probability. H_{hf}: magnetic hyperfine field; $2\varepsilon_Q$: quadrupole shift; δ: center shift (relative to α-Fe at RT); ΔE_Q: quadrupole splitting; Γ full line width at half maximum; RA: relative area.

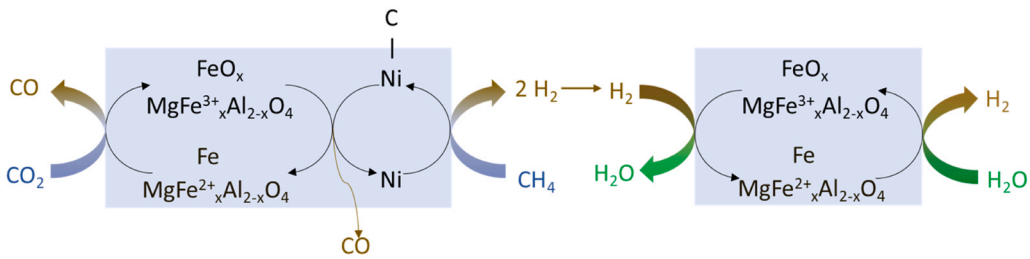

Fig. 11. Schematic representation of the Mars-van Krevelen mechanism proposed for DRM (750 °C, 1 atm) on Ni-Fe/$MgAl_2O_4$ catalysts, accounting for both supported Ni-Fe phases ('Fe' and 'FeO_x') and Fe-substituted $MgAl_2O_4$. Supported metallic Ni and Fe phases are considered part of a Ni-Fe alloy. Side contributions from the water-gas shift reaction are included in the right part of the figure. Blue-grey squares denote the catalyst. Blue arrow sections: DRM reactants; brown arrow sections: DRM products; green arrow section: H_2O contributions from reverse water-gas shift.

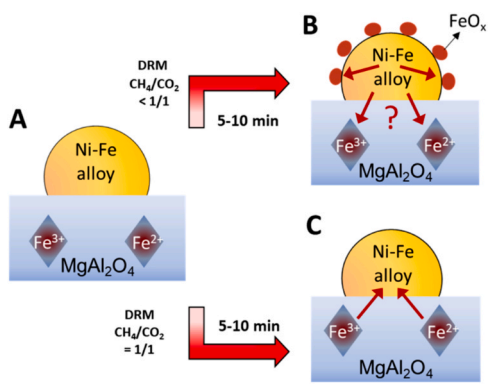

Fig. 12. Schematic representation of the compositional changes of (A) reduced 8Ni5Fe/$MgAl_2O_4$ during DRM (750 °C, 1 atm, 30 min) with (B) $CH_4/CO_2 < 1/1$ and (**C**) $CH_4/CO_2 = 1/1$, as suggested by in situ QXAS. Fe^{3+} and Fe^{2+} denote $MgFe^{3+}{}_xAl_{2-x}O_4$ and $MgFe^{2+}{}_xAl_{2-x}O_4$, respectively. For ease of representation, abstraction is made of $NiAl_2O_4$ and SMSI-related Ni – O bonds. Red arrows in B and C indicate Fe mobility.

(mixed catalyst and support contributions vs. homogeneous bulk) need to be taken into account. Still, the presence of FeO can be deemed plausible, considering previous studies. Hu et al. [67] found FeO to be present in in situ XRD during DRM with $R_c = 1/2$ for a catalyst with higher Fe loading. For the present loading of 5 wt% Fe, no FeO was discerned by in situ XRD until the R_c was set at 1/6 [20], i.e. a far more oxidizing environment. For higher values of R_c, the XRD-amorphous nature of such FeO particles would explain the absence of the phase in the diffraction patterns [20]. Based on the present QXAS and MCR-ALS, an oxidized phase indeed forms. MCR-ALS indicates this oxidation occurs within the first 5–10 min of the reaction, after which the catalyst attains a steady-state composition for DRM. In addition, this oxidation is deeper for lower R_c values as a consequence of the more oxidative environment.

When looking with ex situ TMS after reaction with $R_c = 1/2$, the DRM effect is limited with the alloy RA being slightly lower than after reduction, 58% vs. 62% respectively. When Fe segregates out of the Ni-Fe alloy to the surface under these DRM conditions, the alloy's bulk gets partially depleted of Fe. Even so, due to the broad Ni/Fe ratio of the alloy phase present, it remains in line with component 1 of the MCR-ALS analysis, the unchanged Ni K edge spectra and the Ni-Fe phase diagram [52]. The concomitant change in doublet RA from TMS, 37–42%, is not very large, although if real, it could indicate that part of the extracted Fe gets reincorporated into the support lattice, like in the calcination process. The presence of FeO on the other hand is not resolved, but still possible given the broad signal. Hence, the oxidized iron phase detected by QXAS and MCR-ALS combines small (< 3 nm) FeO_x nanoparticles at the surface of the Ni-Fe alloy core and possibly some $Fe^{2+/3+}$ reincorporated into the support. Both have proven efficiency in carbon mitigation [20,22].

In a more reducing environment ($R_c = 1/1$) (Fig. 12C), sufficient CH_4 dissociation product species are present to counteract oxidation of Fe species by CO_2, leading to unchanged Fe K edge QXAS data. In line with the higher concentrations of reducing CH_4 relative to the case of $R_c = 1/2$, post-reaction TMS and ILEEMS indicate higher contributions of Ni-Fe alloy. Interestingly, TMS post DRM also reveals a higher abundance of Ni-Fe alloy compared to the reduced state. The latter indicates that reduction of the sample was not complete after the H_2-TPR treatment, so that reduction and alloying continued in these DRM reaction conditions, in contrast to reaction with $R_c = 1/2$. This additional alloying under DRM with $R_c = 1/1$ counters Fe extraction from the alloy by CO_2, leading to the very stable performance of 8Ni5Fe/$MgAl_2O_4$ under such conditions, as established previously [20]. The explanation for the insignificant changes at the Ni K edge is analogous to the case of $R_c < 1$.

On the basis of these results, it is proposed that DRM would benefit from the use of higher CH_4/CO_2 ratios as these would avoid Fe segregation from the Ni-Fe alloy, which would otherwise lead to coverage of active Ni sites.

4. Conclusions

The combined use of in situ QXAS and ^{57}Fe Mössbauer spectroscopy has led to novel insights regarding the constituent Ni and Fe phases in 8Ni5Fe/$MgAl_2O_4$ catalysts during H_2-TPR and DRM.

- The Fe phases in the as prepared catalyst have been identified as $NiFe_2O_4$ and $MgFe^{3+}{}_xAl_{2-x}O_4$, while significant Ni contributions have been derived as NiO next to $NiFe_2O_4$.
- Upon H_2-TPR, $NiFe_2O_4$ completely reduces, forming a Ni-Fe alloy, to which quasi-complete reduction of NiO contributes. The $MgFe^{3+}{}_xAl_{2-x}O_4$ phase partially reduces into $MgFe^{2+}{}_xAl_{2-x}O_4$.
- During DRM, the induced changes are dependent on the applied CH_4/CO_2 ratio and can be explained by a Mars-van Krevelen mechanism.
  - o For $CH_4/CO_2 < 1$, a net oxidation of Fe occurs, which extracts it from the Ni-Fe alloy, thereby generating FeO_x nanoparticles that decorate the remainder alloy and possibly even reincorporating some Fe into the support lattice.
  - o For a CH_4/CO_2 ratio = 1, CO_2-induced oxidation is compensated by reduction through product H_2 and CO, leading to ongoing alloying.

This interplay between gas environment and active elements/phases, both in alloy and support, is considered responsible for the DRM performance of 8Ni5Fe/$MgAl_2O_4$.

CRediT authorship contribution statement

Valentijn De Coster: Conceptualization, Methodology, Software, Formal analysis, Writing – original draft, Writing – review & editing. **Nadadur Veeraraghavan Srinath**: Methodology, Formal analysis, Writing – original draft. **Stavros Alexandros Theofanidis**: Investigation, Writing – review & Editing. **Laura Pirro**: Formal analysis, Writing –

original draft. **Antoine Van Alboom**: Mössbauer investigation, Formal analysis, Writing – original draft. **Hilde Poelman**: Conceptualization, Writing – original draft, Writing – review & editing, Supervision, Funding acquisition. **Maarten K. Sabbe**: Supervision. **Guy B. Marin**: Supervision, Funding acquisition. **Vladimir V. Galvita**: Conceptualization, Writing – original draft, Writing – review & editing, Supervision, Funding acquisition.

Declaration of Competing Interest

The authors declare that there are no conflicts of interest.

Acknowledgements

This work was supported by the CALIPSO Trans National Access Program (EU) in supplying financing of subsistence costs for the synchrotron campaign (SOLEIL, France, proposal 201502561). The authors acknowledge support from a public grant overseen by the French National Research Agency (ANR, France) as part of the "Investissements d'Avenir" program (reference: ANR-10-EQPX-45) for the ROCK beamline, as well as the ROCK beamline staff for a smooth beamtime. V.D.C. acknowledges a grant from the Research Fund of Ghent University (BOF; 01D00719, Belgium).

Appendix A. Supporting information

Supplementary data associated with this article can be found in the online version at doi:10.1016/j.apcatb.2021.120720.

References

[1] Q. Zhang, J. Kang, Y. Wang, Development of novel catalysts for fischer–tropsch synthesis: tuning the product selectivity, ChemCatChem 2 (2010) 1030–1058, https://doi.org/10.1002/cctc.201000071.

[2] H. Gruber, P. Groß, R. Rauch, A. Reichhold, R. Zweiler, C. Aichernig, S. Müller, N. Ataimisch, H. Hofbauer, Fischer-Tropsch products from biomass-derived syngas and renewable hydrogen, Biomass Conv. Bioref. (2019), https://doi.org/10.1007/s13399-019-00459-5.

[3] A. Cao, J. Schumann, T. Wang, L. Zhang, J. Xiao, P. Bothra, Y. Liu, F. Abild-Pedersen, J.K. Nørskov, Mechanistic insights into the synthesis of higher alcohols from syngas on CuCo alloys, ACS Catal. 8 (2018) 10148–10155, https://doi.org/10.1021/acscatal.8b01596.

[4] G.A. Olah, A. Goeppert, M. Czaun, G.K.S. Prakash, Bi-reforming of methane from any source with steam and carbon dioxide exclusively to metgas (CO–2H2) for methanol and hydrocarbon synthesis, J. Am. Chem. Soc. 135 (2013) 648–650, https://doi.org/10.1021/ja311796n.

[5] EIA., Annual Energy Outlook 2019, in: U.S.Do Energy (Ed.) U.S. Energy Information Administration: Washington, D.C., April, 2019.

[6] S.D. Angeli, L. Turchetti, G. Monteleone, A.A. Lemonidou, Catalyst development for steam reforming of methane and model biogas at low temperature, Appl. Catal. B Environ. 181 (2016) 34–46, https://doi.org/10.1016/j.apcatb.2015.07.039.

[7] J.L. Rogers, M.C. Mangarella, A.D. D'Amico, J.R. Gallagher, M.R. Dutzer, E. Stavitski, J.T. Miller, C. Sievers, Differences in the nature of active sites for methane dry reforming and methane steam reforming over nickel aluminate catalysts, ACS Catal. 6 (2016) 5873–5886, https://doi.org/10.1021/acscatal.6b01133.

[8] S. Ayabe, H. Omoto, T. Utaka, R. Kikuchi, K. Sasaki, Y. Teraoka, K. Eguchi, Catalytic autothermal reforming of methane and propane over supported metal catalysts, Appl. Catal. A Gen. 241 (2003) 261–269, https://doi.org/10.1016/S0926-860X(02)00471-4.

[9] M. Luneau, E. Gianotti, N. Guilhaume, E. Landrivon, F.C. Meunier, C. Mirodatos, Y. Schuurman, Experiments and modeling of methane autothermal reforming over structured Ni–Rh-based Si-SiC foam catalysts, Ind. Eng. Chem. Res. 56 (2017) 13165–13174, https://doi.org/10.1021/acs.iecr.7b01559.

[10] S. Chen, L. Zeng, H. Tian, X. Li, J. Gong, Enhanced lattice oxygen reactivity over Ni-modified WO3-based redox catalysts for chemical looping partial oxidation of methane, ACS Catal. 7 (2017) 3548–3559, https://doi.org/10.1021/acscatal.7b00436.

[11] D. Kang, M. Lee, H.S. Lim, J.W. Lee, Chemical looping partial oxidation of methane with CO_2 utilization on the ceria-enhanced mesoporous Fe2O3 oxygen carrier, Fuel 215 (2018) 787–798, https://doi.org/10.1016/j.fuel.2017.11.106.

[12] S.A. Theofanidis, R. Batchu, V.V. Galvita, H. Poelman, G.B. Marin, Carbon gasification from Fe–Ni catalysts after methane dry reforming, Appl. Catal. B: Environ. 185 (2016) 42–55, https://doi.org/10.1016/j.apcatb.2015.12.006.

[13] I. Luisetto, S. Tuti, E. Di Bartolomeo, Co and Ni supported on CeO2 as selective bimetallic catalyst for dry reforming of methane, Int. J. Hydrog. Energy 37 (2012) 15992–15999, https://doi.org/10.1016/j.ijhydene.2012.08.006.

[14] S. Damyanova, B. Pawelec, K. Arishtirova, J.L.G. Fierro, Ni-based catalysts for reforming of methane with CO_2, Int. J. Hydrog. Energy 37 (2012) 15966–15975, https://doi.org/10.1016/j.ijhydene.2012.08.056.

[15] L. Wang, D. Li, M. Koike, S. Koso, Y. Nakagawa, Y. Xu, K. Tomishige, Catalytic performance and characterization of Ni-Fe catalysts for the steam reforming of tar from biomass pyrolysis to synthesis gas, Appl. Catal. A: Gen. 392 (2011) 248–255, https://doi.org/10.1016/j.apcata.2010.11.013.

[16] D. Tian, Z. Liu, D. Li, H. Shi, W. Pan, Y. Cheng, Bimetallic Ni-Fe total-methanation catalyst for the production of substitute natural gas under high pressure, Fuel 104 (2013) 224–229, https://doi.org/10.1016/j.fuel.2012.08.033.

[17] A. More, S. Bhavsar, G. Veser, Iron–nickel alloys for carbon dioxide activation by chemical looping dry reforming of methane, Energy Technol. 4 (2016) 1147–1157, https://doi.org/10.1002/ente.201500539.

[18] S. Sitthisa, W. An, D.E. Resasco, Selective conversion of furfural to methylfuran over silica-supported NiFe bimetallic catalysts, J. Catal. 284 (2011) 90–101, https://doi.org/10.1016/j.jcat.2011.09.005.

[19] S.M. Kim, P.M. Abdala, T. Margossian, D. Hosseini, L. Foppa, A. Armutlulu, W. van Beek, A. Comas-Vives, C. Copéret, C. Müller, Cooperativity and dynamics increase the performance of NiFe dry reforming catalysts, J. Am. Chem. Soc. 139 (2017) 1937–1949, https://doi.org/10.1021/jacs.6b11487.

[20] S.A. Theofanidis, V.V. Galvita, H. Poelman, G.B. Marin, Enhanced carbon-resistant dry reforming Fe-Ni catalyst: role of Fe, ACS Catal. 5 (2015) 3028–3039, https://doi.org/10.1021/acscatal.5b00357.

[21] J. Hu, H. Poelman, G.B. Marin, C. Detavernier, S. Kawi, V.V. Galvita, FeO controls the sintering of iron-based oxygen carriers in chemical looping CO_2 conversion, J. CO2 Util. 40 (2020), 101216, https://doi.org/10.1016/j.jcou.2020.101216.

[22] S.A. Theofanidis, V.V. Galvita, H. Poelman, N.V.R.A. Dharanipragada, A. Longo, M. Meledina, G. Van Tendeloo, C. Detavernier, G.B. Marin, Fe-containing magnesium aluminate support for stability and carbon control during methane reforming, ACS Catal. 8 (2018) 5983–5995, https://doi.org/10.1021/acscatal.8b01039.

[23] N.V.R.A. Dharanipragada, L.C. Buelens, H. Poelman, E. De Grave, V.V. Galvita, G. B. Marin, Mg–Fe–Al–O for advanced CO_2 to CO conversion: carbon monoxide yield vs. oxygen storage capacity, J. Mater. Chem. A 3 (2015) 16251–16262, https://doi.org/10.1039/C5TA02289D.

[24] N.V.R.A. Dharanipragada, V.V. Galvita, H. Poelman, L.C. Buelens, G.B. Marin, A. Longo, Insight in kinetics from pre-edge features using time resolved in situ XAS, AIChE J. 64 (2018) 1339–1349, https://doi.org/10.1002/aic.16017.

[25] J. Stötzel, D. Luetzenkirchen-Hecht, R. Frahm, A new flexible monochromator setup for quick scanning X-ray absorption spectroscopy, Rev. Sci. Instrum. 81 (2010), 073109, https://doi.org/10.1063/1.3458015.

[26] V. Briois, C. Fontaine, S. Belin, L. Barthe, T. Moreno, V. Pinty, A. Carcy, R. Girardot, E. Fonda, ROCK: the new Quick-EXAFS beamline at SOLEIL, J. Phys. Conf. Ser. 712 (2016), 012149, https://doi.org/10.1088/1742-6596/712/1/012149.

[27] C. Lesage, E. Devers, C. Legens, G. Fernandes, O. Roudenko, V. Briois, High pressure cell for edge jumping X-ray absorption spectroscopy: applications to industrial liquid sulfidation of hydrotreatment catalysts, Catal. Today 336 (2019) 63–73, https://doi.org/10.1016/j.cattod.2019.01.081.

[28] B. Ravel, M. Newville, ATHENA, ARTEMIS, HEPHAESTUS: data analysis for X-ray absorption spectroscopy using IFEFFIT, J. Synchrotron Radiat. 12 (2005) 537–541, https://doi.org/10.1107/S0909049505012719.

[29] A. Manceau, M. Marcus, T. Lenoir, Estimating the number of pure chemical components in a mixture by x-ray absorption spectroscopy, J. Synchrotron Radiat. 21 (2014) 1140–1147, https://doi.org/10.1107/S1600577514013526.

[30] C. Nayak, D. Bhattacharyya, S.N. Jha, N.K. Sahoo, In situ XAS study on growth of PVP-stabilized Cu nanoparticles, ChemistrySelect 3 (2018) 7370–7377, https://doi.org/10.1002/slct.201801358.

[31] J. Jaumot, A. de Juan, R. Tauler, MCR-ALS GUI 2.0: new features and applications, Chemom. Intell. Lab. Syst. 140 (2015) 1–12, https://doi.org/10.1016/j.chemolab.2014.10.003.

[32] E. De Grave, R.E. Vandenberghe, C. Dauwe, ILEEMS: methodology and applications to iron oxides, Hyperfine Inter. 161 (2005) 147–160, https://doi.org/10.1007/s10751-005-9177-1.

[33] T.E. Westre, P. Kennepohl, J.G. DeWitt, B. Hedman, K.O. Hodgson, E.I. Solomon, A multiplet analysis of Fe K-Edge 1s → 3d pre-edge features of iron complexes, J. Am. Chem. Soc. 119 (1997) 6297–6314, https://doi.org/10.1021/ja964352a.

[34] D. Zhou, S. Permien, J. Rana, M. Krengel, F. Sun, G. Schumacher, W. Bensch, J. Banhart, Investigation of electronic and local structural changes during lithium uptake and release of nano-crystalline NiFe2O4 by X-ray absorption spectroscopy, J. Power Sources 342 (2017) 56–63, https://doi.org/10.1016/j.jpowsour.2016.12.038.

[35] K.C. Galbreath, R.L. Schulz, D.L. Toman, C.M. Nyberg, F.E. Huggins, G.P. Huffman, E.J. Zillioux, Nickel and sulfur speciation of residual oil fly ashes from two electric utility steam-generating units, J. Air Waste Manag. Assoc. 55 (2005) 309–318, https://doi.org/10.1080/10473289.2005.10464626.

[36] L.C. Buelens, A. Van Alboom, H. Poelman, C. Detavernier, G.B. Marin, V.V. Galvita, Fe2O3–MgAl2O4 for CO production from CO_2: mössbauer spectroscopy and in situ X-ray diffraction, ACS Sustain. Chem. Eng. (2019), https://doi.org/10.1021/acssuschemeng.9b01036.

[37] A.-F. Lehlooh, J. Amighian, S. Mahmood, Mössbauer spectroscopy study of aluminium substituted nickel-ferrites, Hyperfine Inter. 183 (2008) 193–198, https://doi.org/10.1007/s10751-008-9751-4.

[38] P. Coquay, G. E, R. Vandenberghe, C. Dauwe, E. Flahaut, C. Laurent, A. Peigney, A. Rousset, Mossbauer spectroscopy study of MgAl2O4-matrix nanocomposite

powders containing carbon nanotubes and iron-based nanoparticles, Acta Mater. 48 (2000) 3015–3023, https://doi.org/10.1016/S1359-6454(00)00063-X.
[39] E. De Grave, R.E. Vandenberghe, Mössbauer effect study of the spin structure in natural hematites, Phys. Chem. Miner. 17 (1990) 344–352, https://doi.org/10.1007/BF00200130.
[40] S.A. Theofanidis, V.V. Galvita, M. Sabbe, H. Poelman, C. Detavernier, G.B. Marin, Controlling the stability of a Fe–Ni reforming catalyst: structural organization of the active components, Appl. Catal. B Environ. 209 (2017) 405–416, https://doi.org/10.1016/j.apcatb.2017.03.025.
[41] S.A. Theofanidis, R. Batchu, V.V. Galvita, H. Poelman, G.B. Marin, Carbon gasification from Fe-Ni catalysts after methane dry reforming, Appl. Catal. B: Environ. 185 (2016) 42–55, https://doi.org/10.1016/j.apcatb.2015.12.006.
[42] C.-J. Pan, M.-C. Tsai, W.-N. Su, J. Rick, N.G. Akalework, A.K. Agegnehu, S.-Y. Cheng, B.-J. Hwang, Tuning/exploiting strong metal-support interaction (SMSI) in heterogeneous catalysis, J. Taiwan Inst. Chem. Eng. 74 (2017) 154–186, https://doi.org/10.1016/j.jtice.2017.02.012.
[43] S. Corthals, J. Van Nederkassel, J. Geboers, H. De Winne, J. Van Noyen, B. Moens, B. Sels, P. Jacobs, Influence of composition of MgAl2O4 supported NiCeO2ZrO2 catalysts on coke formation and catalyst stability for dry reforming of methane, Catal. Today 138 (2008) 28–32, https://doi.org/10.1016/j.cattod.2008.04.038.
[44] D.S. Park, Z. Li, H. Devianto, H.-I. Lee, Characteristics of alkali-resistant Ni/MgAl2O4 catalyst for direct internal reforming molten carbonate fuel cell, Int. J. Hydrog. Energy 35 (2010) 5673–5680, https://doi.org/10.1016/j.ijhydene.2010.03.043.
[45] X. Feng, J. Liu, P. Zhang, Q. Zhang, L. Xu, L. Zhao, X. Song, L. Gao, Highly coke resistant Mg–Ni/Al2O3 catalyst prepared via a novel magnesiothermic reduction for methane reforming catalysis with CO_2: the unique role of Al–Ni intermetallics, Nanoscale 11 (2019) 1262–1272, https://doi.org/10.1039/C8NR08447E.
[46] Q.L.M. Ha, H. Lund, C. Kreyenschulte, S. Bartling, H. Atia, T.H. Vuong, S. Wohlrab, U. Armbruster, Development of highly stable low Ni content catalyst for dry reforming of CH4-rich feedstocks, ChemCatChem 12 (2020) 1562–1568, https://doi.org/10.1002/cctc.201902066.
[47] B. Yan, S. Yao, S. Kattel, Q. Wu, Z. Xie, E. Gomez, P. Liu, D. Su, J.G. Chen, Active sites for tandem reactions of CO_2 reduction and ethane dehydrogenation, Proc. Natl. Acad. Sci. U. S. A. 115 (2018) 8278–8283, https://doi.org/10.1073/pnas.1806950115.
[48] C. Ruckebusch, A. De Juan, L. Duponchel, J.P. Huvenne, Matrix augmentation for breaking rank-deficiency: a case study, Chemom. Intell. Lab. Syst. 80 (2006) 209–214, https://doi.org/10.1016/j.chemolab.2005.06.009.
[49] Z. Ma, D. Zeng, S. Zhang, R. Xiao, Effect of supports on the redox performance of NiFe2O4 in a chemical looping process, Energy Technol. 7 (2019), 1900374, https://doi.org/10.1002/ente.201900374.
[50] L. Zhou, L. Li, N. Wei, J. Li, J.-M. Basset, Effect of NiAl2O4 formation on Ni/Al2O3 stability during dry reforming of methane, ChemCatChem 7 (2015) 2508–2516, https://doi.org/10.1002/cctc.201500379.
[51] T.E. Cranshaw, The electronic and magnetic structure of ordered Ni3Fe studied by Mossbauer spectroscopy, J. Phys. F: Met. Phys. 17 (1987) 967–984, https://doi.org/10.1088/0305-4608/17/4/022.
[52] G. Cacciamani, J. De Keyzer, R. Ferro, U.E. Klotz, J. Lacaze, P. Wollants, Critical evaluation of the Fe–Ni, Fe–Ti and Fe–Ni–Ti alloy systems, Intermetallics 14 (2006) 1312–1325, https://doi.org/10.1016/j.intermet.2005.11.028.
[53] C.E. Johnson, M.S. Ridout, T.E. Cranshaw, The mössbauer effect in iron alloys, Proc. Phys. Soc. 81 (1963) 1079–1090, https://doi.org/10.1088/0370-1328/81/6/313.
[54] R. Benrabaa, H. Boukhlouf, A. Löfberg, A. Rubbens, R.-N. Vannier, E. Bordes-Richard, A. Barama, Nickel ferrite spinel as catalyst precursor in the dry reforming of methane: synthesis, characterization and catalytic properties, J. Nat. Gas. Chem. 21 (2012) 595–604, https://doi.org/10.1016/S1003-9953(11)60408-8.
[55] M. Chamoumi, N. Abatzoglou, NiFe2O4 production from α-Fe2O3 via improved solid state reaction: application as catalyst in CH4 dry reforming, Can. J. Chem. Eng. 94 (2016) 1801–1808, https://doi.org/10.1002/cjce.22561.
[56] Y. Zhang, W. Wei, X. Yang, F. Wei, Reduction of Fe and Ni in Fe-Ni-O systems, J. Min. Metall. Sect. B Metall. 49 (2013) 13–20, https://doi.org/10.2298/JMMB120208038Z.
[57] N.V.R.A. Dharanipragada, V.V. Galvita, H. Poelman, L.C. Buelens, C. Detavernier, G.B. Marin, Bifunctional Co- and Ni- ferrites for catalyst-assisted chemical looping with alcohols, Appl. Catal. B Environ. 222 (2018) 59–72, https://doi.org/10.1016/j.apcatb.2017.09.067.
[58] A. Longo, S.A. Theofanidis, C. Cavallari, N.V. Srinath, J. Hu, H. Poelman, M. K. Sabbe, C.J. Sahle, G.B. Marin, V.V. Galvita, What makes Fe-modified MgAl2O4 an active catalyst support? Insight from X-ray raman scattering, ACS Catal. 10 (2020) 6613–6622, https://doi.org/10.1021/acscatal.0c00759.
[59] S. Andraos, R. Abbas-Ghaleb, D. Chlala, A. Vita, C. Italiano, M. Laganà, L. Pino, M. Nakhl, S. Specchia, Production of hydrogen by methane dry reforming over ruthenium-nickel based catalysts deposited on Al2O3, MgAl2O4, and YSZ, Int. J. Hydrog. Energy 44 (2019) 25706–25716, https://doi.org/10.1016/j.ijhydene.2019.08.081.
[60] S. Katheria, A. Gupta, G. Deo, D. Kunzru, Effect of calcination temperature on stability and activity of Ni/MgAl2O4 catalyst for steam reforming of methane at high pressure condition, Int. J. Hydrog. Energy 41 (2016) 14123–14132, https://doi.org/10.1016/j.ijhydene.2016.05.109.
[61] L. Azancot, L.F. Bobadilla, J.L. Santos, J.M. Córdoba, M.A. Centeno, J.A. Odriozola, Influence of the preparation method in the metal-support interaction and reducibility of Ni-Mg-Al based catalysts for methane steam reforming, Int. J. Hydrog. Energy 44 (2019) 19827–19840, https://doi.org/10.1016/j.ijhydene.2019.05.167.
[62] A. Lak, M. Kraken, F. Ludwig, A. Kornowski, D. Eberbeck, S. Sievers, F.J. Litterst, H. Weller, M. Schilling, Size dependent structural and magnetic properties of FeO–Fe3O4 nanoparticles, Nanoscale 5 (2013) 12286–12295, https://doi.org/10.1039/C3NR04562E.
[63] V.V. Galvita, H. Poelman, C. Detavernier, G.B. Marin, Catalyst-assisted chemical looping for CO_2 conversion to CO, Appl. Catal. B: Environ. 164 (2015) 184–191, https://doi.org/10.1016/j.apcatb.2014.09.007.
[64] J.C. Bauer, X. Chen, Q. Liu, T.-H. Phan, R.E. Schaak, Converting nanocrystalline metals into alloys and intermetallic compounds for applications in catalysis, J. Mater. Chem. 18 (2008) 275–282, https://doi.org/10.1039/B712035D.
[65] S.A. Theofanidis, H. Poelman, G.B. Marin, V.V. Galvita, Chapter 6 - how does the surface structure of Ni-Fe nanoalloys control carbon formation during methane steam/dry reforming? in: V.A. Sadykov (Ed.), Advanced Nanomaterials for Catalysis and Energy Elsevier Inc, Amsterdam, 2019, pp. 177–225.
[66] S.A. Theofanidis, V.V. Galvita, C. Konstantopoulos, H. Poelman, G.B. Marin, Fe-based nano-materials in catalysis, Materials 11 (2018), https://doi.org/10.3390/ma11050831.
[67] J. Hu, L. Buelens, S.-A. Theofanidis, V.V. Galvita, H. Poelman, G.B. Marin, CO_2 conversion to CO by auto-thermal catalyst-assisted chemical looping, J. CO2 Util. 16 (2016) 8–16, https://doi.org/10.1016/j.jcou.2016.05.006.